Open access • Journal Article • DOI:10.1038/S41586-020-2753-3

Bolometer operating at the threshold for circuit quantum electrodynamics

Roope Kokkoniemi, Jean-Philippe Girard, Dibyendu Hazra, Antti Laitinen ...+6 more authors

Published on: 11 Aug 2020 - arXiv: Mesoscale and Nanoscale Physics

Topics: Circuit quantum electrodynamics, Quantum technology, Quantum noise, Qubit and Quantum computer

Department of applied physics

Bolometric techniques for circuit quantum electrodynamics

Roope Kokkoniemi

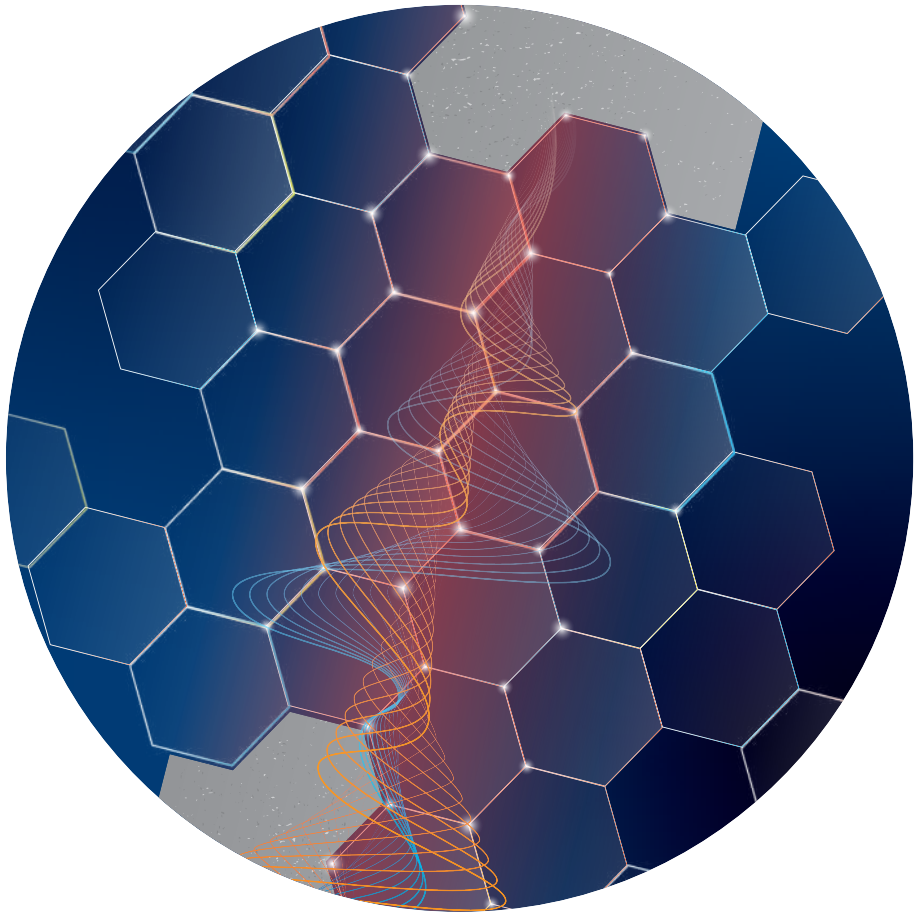

Aalto University

DOCTORAL DISSERTATIONS

Aalto University publication series
DOCTORAL DISSERTATIONS 203/2020

Bolometric techniques for circuit quantum electrodynamics

Roope Kokkoniemi

A doctoral dissertation completed for the degree of Doctor of Science (Technology) to be defended, with the permission of the Aalto University School of Science, at https://aalto.zoom.us/j/63398870897 on 4 December 2020 at noon.

Aalto University
School of Science
Department of applied physics
Quantum Computing and Devices

Supervising professor
Professor Mikko Möttönen, Aalto University, Finland

Thesis advisor
Dr. Jean-Philippe Girard, Aalto University, Finland

Preliminary examiners
Professor Hervé Courtois, Université Grenoble Alpes, France
Dr. Kirill Fedorov, Walther-Meißner-Institut, Germany

Opponent
Professor Ilari Maasilta, University of Jyväskylä, Finland

Aalto University publication series
DOCTORAL DISSERTATIONS 203/2020

ISBN 978-952-64-0170-6 (printed)
ISBN 978-952-64-0171-3 (pdf)
ISSN 1799-4934 (printed)
ISSN 1799-4942 (pdf)
http://urn.fi/URN:ISBN:978-952-64-0171-3

Images: Cover image: Marianne LENOIR

Unigrafia Oy
Helsinki 2020

Finland

NORDIC SWAN ECOLABEL
Printed matter
4041-0619

Aalto University

Abstract

Aalto University, P.O. Box 11000, FI-00076 Aalto www.aalto.fi

Author
Roope Kokkoniemi

Name of the doctoral dissertation
Bolometric techniques for circuit quantum electrodynamics

Publisher School of Science

Unit Department of applied physics

Series Aalto University publication series DOCTORAL DISSERTATIONS 203/2020

Field of research Engineering Physics

Manuscript submitted 17 September 2020 **Date of the defence** 4 December 2020

Permission for public defence granted (date) 11 November 2020 **Language** English

☐ **Monograph** ☒ **Article dissertation** ☐ **Essay dissertation**

Abstract

Superconducting quantum bits, or qubits, provide a promising platform for realizing large-scale quantum computers. As the number of qubits on a chip keeps increasing, so does the amount of required electronics and instruments needed for qubit control and readout. Eventually, it will be impossible to fit all the control lines into a cryostat. Therefore, there is an on-going effort to move the conventional room-temperature components into the lower-temperature stages. So-called Josephson junction is one of the fundamental building blocks used to realize these components in superconducting circuits.

In this thesis, we study a particular type of a Josephson junction, a superconductor—normal-metal—superconductor junction. We experimentally measure its admittance at typical frequencies used in superconducting circuits. Furthermore, we show theoretically and experimentally that Josephson junctions can be used to realize one of the components aiding in scaling up quantum computers, a magnetic-flux-tunable phase shifter.

The main topic of this thesis is bolometry. It is one of the oldest forms of thermal radiation detection invented over a century ago. Yet, it remains as a tool-of-choice in many applications ranging from consumer electronics to particle physics and astronomy. State-of-the-art bolometers have noise equivalent power (NEP) of 300 zW$\sqrt{\text{Hz}}$ and can detect single 1.6-THz photons, which corresponds to the energy of 1.1 zJ. However, superconducting quantum computers utilize light at microwave frequencies in their operation. Thermal detectors have yet to reach this frontier due to orders of magnitude lower energy of the microwave photons than far-infrared photons.

In this thesis, we bring the performance of bolometers deep into the microwave regime. First, we study a gold-palladium-nanowire-based bolometer. We are able to decrease the NEP record down to 50 zW$\sqrt{\text{Hz}}$. By introducing a Josephson parametric amplifier to the measurement circuitry, we can further improve the NEP to 20 zW$\sqrt{\text{Hz}}$. Together with the low thermal time constant below 100 μs, this result indicates an energy resolution of 0.32 zJ. Second, we investigate graphene as a substitute for gold-palladium. Graphene is a promising candidate for bolometry due to its two-dimensional nature. We find NEP on par with the gold-palladium bolometer. Importantly, the thermal time constant with graphene is about two orders of magnitude shorter, which implies an energy resolution of 20 yJ, corresponding to the energy of a single 30-GHz photon.

Keywords Bolometry, cQED, quantum computing

ISBN (printed) 978-952-64-0170-6 **ISBN (pdf)** 978-952-64-0171-3

ISSN (printed) 1799-4934 **ISSN (pdf)** 1799-4942

Location of publisher Helsinki **Location of printing** Helsinki **Year** 2020

Pages 149 **urn** http://urn.fi/URN:ISBN:978-952-64-0171-3

Tekijä
Roope Kokkoniemi

Väitöskirjan nimi
Bolometric techniques for circuit quantum electrodynamics

Julkaisija Perustieteiden korkeakoulu

Yksikkö Teknillisen fysiikan laitos

Sarja Aalto University publication series DOCTORAL DISSERTATIONS 203/2020

Tutkimusala Teknillinen fysiikka

Käsikirjoituksen pvm 17.09.2020 **Väitöspäivä** 04.12.2020

Väittelyluvan myöntämispäivä 11.11.2020 **Kieli** Englanti

☐ **Monografia** ☒ **Artikkeliväitöskirja** ☐ **Esseeväitöskirja**

Tiivistelmä

Suprajohtava kvanttibitti, eli qubitti, on lupaava alusta suuren mittakaavan kvanttitietokoneen toteuttamiselle. Qubittien ohjaamiseen ja lukemiseen tarvittavan elektroniikan ja instrumenttien lukumäärä kasvaa käsi kädessä yhdelle piisirulle ladottujen toimivien qubittien lukumäärän kanssa. Tämän vuoksi kvanttitietokoneiden rakentamisessa tulee eteen väistämättä tilanne, jossa kaikki ohjauslinjat eivät mahdu kryostaattiin. Tästä syystä suuri määrä kansainvälisen tutkimuksen resursseja on keskitetty perinteisten huoneen lämmössä toimivien komponenttien siirtämiseksi mataliin lämpötiloihin. Keskeinen rakennuspala näiden komponenttien toteuttamisessa suprajohtavissa virtapiireissä on niin sanottu Josephsonin liitos.

Tässä väitöskirjassa tutkitaan tarkemmin erästä Josephsonin liitoksen tyyppiä, suprajohde-normaalimetalli-suprajohde liitosta. Mittaamme tällaisen liitoksen admittanssin taajuuksilla, joita tyypillisesti käytetään suprajohtavissa piireissä. Työssä myös osoitetaan teoreettisesti ja kokeellisesti, että Josephsonin liitoksilla voidaan rakentaa magneettikentällä säädettävä vaihesiirrin, joka on yksi apukomponenteista suuren mittakaavan kvanttitietokoneessa.

Tämän väitöskirjan pääaihe on bolometria. Se on yli vuosisata sitten keksitty tekniikka säteilyn ilmaisemiseen epäsuorasti mittaamalla lämpötilan muutosta. Korkeasta iästä huolimatta tekniikka on edelleen laajassa käytössä aina kuluttajaelektroniikasta hiukkasfysiikkaan ja astronomiaan. Huippuluokan bolometrien kohinaa vastaava teho (NEP) on 300 zW$\sqrt{\text{Hz}}$ ja niillä voidaan havaita yksittäisiä 1.6 THz:n fotoneita, mikä vastaa 1.1 zJ:n energiaa. Suprajohtavat kvanttitietokoneet käyttävät mikroaaltotaajuuden fotoneita toiminnassaan. Tätä rajapyykkiä bolometrit eivät ole vielä saavuttaneet sillä näiden mikroaaltofotonien energia on kertaluokkia pienempi kuin infrapunafotonien.

Tässä väitöskirjassa viedään bolometrien suorituskyky syvälle mikroaaltoalueelle. Kulta-palladium nanolankaan perustuvalla bolometrilla kohinaa vastaavan tehon ennätystä pienennetään lukemaan 50 zW/$\sqrt{\text{Hz}}$. Lisäämällä mittapiiriin Josephsonin parametrinen vahvistin, kohinaa vastaava teho pienenee edelleen lukemaan 20 zW/$\sqrt{\text{Hz}}$. Yhdessä matalan termisen aikavakion kanssa tuloksista voidaan laskea energiaresoluutioksi 0.32 zJ. Lisäksi väitöskirjassa tutkitaan grafeeniin perustuvaa bolometria. Grafeeni on lupaava vaihtoehto metallille sen kaksiulotteisen rakenteen vuoksi. Kohinaa vastaavan tehon mitataan olevan samaa luokkaa kulta-palladium bolometrin kanssa, mutta terminen aikavakio on kaksi kertaluokkaa lyhyempi. Tämä indikoi energiaresoluution olevan 20 yJ, mikä vastaa yhden 30 GHz:n fotonin energiaa.

Avainsanat Bolometria, cQED, kvanttilaskenta

ISBN (painettu) 978-952-64-0170-6 **ISBN (pdf)** 978-952-64-0171-3

ISSN (painettu) 1799-4934 **ISSN (pdf)** 1799-4942

Julkaisupaikka Helsinki **Painopaikka** Helsinki **Vuosi** 2020

Sivumäärä 149 **urn** http://urn.fi/URN:ISBN:978-952-64-0171-3

Preface

The work presented in this thesis was carried out in the Quantum Computing and Devices group, or QCD Labs, at the Department of Applied Physics, Aalto University, between the years 2016 and 2020.

First of all, I wish to thank my supervising professor Mikko Möttönen, leader of the QCD group, for giving me the opportunity to work in the group on my BSc, MSc, and Ph.D. theses. It was a true pleasure to work under his guidance for all those years. His vast knowledge never ceases to amaze me, and I can only hope that some fraction of it absorbed into me during my stay at QCD. I wish to also thank Prof. Jukka Pekola, leader of the PICO group, who acted as my official supervisor for the first two years of my Ph.D. studies. He always reassured me that my studies were progressing on time, even if I didn't feel like they were.

I joined the QCD group in 2015 as a bachelor's thesis student. My first point of contact was Russell Lake. I thank him for introducing me to the group and the world of experimental low-temperature physics. I started my Ph.D. studies in 2016. The topic of bolometry was foreign to me and as at the beginning of every endeavor, it seemed very confusing. Fortunately, I had the privilege of learning from Joonas Govenius. His excellent guidance through those first few crucial months made the rest of them seem less daunting. Early in my studies, I also had the opportunity to work with Visa Vesterinen, to whom I'm grateful for guiding me deeper into the world of bolometry. The two people who I probably bugged the most with my questions, ranging from setting up experiments to how to keep the lab from self-destructing, are Matti Partanen and Máté Jenei. It was a true pleasure working with them for many years. I wish to also thank Jean-Philippe Girard for acting as my official advisor. I had the pleasure of working with him for the final year of my studies.

I'm also thankful for the present and former members of QCD, including, but not limited to, Joni, Sofia, Jinli, Tuomas, Dibyendu, Wei, Valtteri, Tianyi, Chengyu, Kuan, Jan, Arto, Roberto, Kostya, Aarne, Marci, Vasilii V., Vasilii S., Timm, Giacomo, Johannes, Akseli, Suman, and Sasu. Throughout my Ph.D. studies, I had the pleasure of instructing several bright

students; Osama Abuzaid, Eemil Visakorpi, Iiro Sallinen, and Kassius Kohvakka. Their enthusiasm is something I can only hope to achieve one day. I wish to also thank our upstairs neighbors, the PICO group and especially Elsa Mannila and Joonas Peltonen, for our on-going collaboration.

I wish to acknowledge the Finnish Cultural Foundation for providing me the financial support for my Ph.D. studies, and Doctoral Education Network in Condensed Matter and Materials Physics for supporting my conference and summer school trips.

Finally, I'm grateful for having such a wonderful family who have supported me throughout my lengthy studies, and my girlfriend Marika who has brought balance into my life. I wish to also thank my cats, Hunska, who tirelessly supervised me throughout the COVID19 pandemic, and Kerri, who unfortunately recently passed away. May your eternal hunt be wild and servants obedient. What would life be without friends? I wish to thank all my friends for providing me occasional escape from the daily grind.

Helsinki, November 16, 2020,

Roope Kokkoniemi

Contents

List of Publications

This thesis consists of an overview and of the following publications which are referred to in the text by their Roman numerals.

I R. E. Lake, J. Govenius, R. Kokkoniemi, K. Y. Tan, M. Partanen, P. Virtanen, and M. Möttönen. Microwave Admittance of Gold-Palladium Nanowires with Proximity-Induced Superconductivity. *Advanced Electronic Materials*, **3**, 1600227, March 2017.

II R. Kokkoniemi, T. Ollikainen, R. E. Lake, S. Saarenpää, K. Y. Tan, J. I. Kokkala, C. B. Dağ, J. Govenius, and M. Möttönen. Flux-tunable phase shifter for microwaves. *Scientific Reports*, **7**, 1, November 2017.

III J. Zhang, T. Li, R. Kokkoniemi, C. Yan, W. Liu, M. Partanen, K. Y. Tan, M. He, L. Ji, L. Grönberg, and M. Möttönen.. Broadband Tunable Phase Shifter For Microwaves.. *AIP Advances*, **10**, 065128, June 2020.

IV R. Kokkoniemi, J. Govenius, V. Vesterinen, R. E. Lake, A. M. Gunyhó, K. Y. Tan, S. Simbierowicz, L. Grönberg, J. Lehtinen, M. Prunnila, J. Hassel, A. Lamminen, O.-P. Saira, and M. Möttönen. Nanobolometer with ultralow noise equivalent power. *Communications Physics*, **2**, 1, October 2019.

V R. Kokkoniemi, J.-P. Girard, D. Hazra, A. Laitinen, J. Govenius, R. E. Lake, I. Sallinen, V. Vesterinen, M. Partanen, J. Y. Tan, K. W. Chan, K. Y. Tan, P. Hakonen, and M. Möttönen. Bolometer operating at the threshold for circuit quantum electrodynamics. *Nature*, **586**, 47, September 2020.

Author's Contribution

Publication I: "Microwave Admittance of Gold-Palladium Nanowires with Proximity-Induced Superconductivity"

Samples were designed by R. E. L. and J.G. Fabrication was carried by R. E. L. and J. G. with assistance from K. Y. T. Measurements were performed mostly by R. E. L. with contributions from J. G. and M. P. Data analysis was conducted by R. K., R. E. L., and J. G. Circuit model calculations were carried out by R. K. with help from R. E. L. and J. G. Theoretical calculation concerning the Usadel equations were done by P. V. The manuscript was mostly written by R. E. L. and J. G. with comments from all authors. The work was supervised by M. M.

Publication II: "Flux-tunable phase shifter for microwaves"

R.K. conducted the experiments, analyzed the data and participated in theoretical analysis and writing the manuscript. T.O. participated in preparing the manuscript. R.E.L. participated in designing the measurement setup and the experimental sample. S.S. participated in designing the sample. K.Y.T. fabricated the sample. J.I.K. and C.B.D. conducted theoretical studies. J.G. participated in designing the measurement setup. M.M. supervised the work and participated in writing of the manuscript.

Publication III: "Broadband Tunable Phase Shifter For Microwaves."

J.Z. designed the sample with input from R.K. The fabrication was carried out mostly by T.L. with minor contributions from W. L. and L.G. The measurements and simulations were conducted by J.Z. with assistance from R.K., C.Y., M.P., and K.Y.T. The work was supervised by M. H., L. J.,

and M.M.

Publication IV: "Nanobolometer with ultralow noise equivalent power"

R.K. participated in the measurements and data analysis. V.V. integrated the JPA to the measurement setup, and participated to the measurements and data analysis. J.G., K.Y.T. and R.E.L. developed the fabrication process for the detector sample. J.G. and R.E.L. designed and fabricated the detector sample. J.G. designed the measurement setup. A.M.G. carried out preliminary measurements with J.G. The lens antenna simulations and terahertz detection rate computations were carried out by A.L. and J.H. All authors have contributed to preparing the manuscript, although most of the work was carried out by R.K., J.G., V.V. and M.M. In addition, V.V., S.S., L.G., J.L., M.P., J.H. and O.-P.S. provided the JPA and M.M. supervised the work in general.

Publication V: "Bolometer operating at the threshold for circuit quantum electrodynamics"

R. K. and J.-P. G. conducted the experiments and data analysis of the main article. The main sample was designed by R. E. L. and fabricated by D. H. and A. L. Initial characterizations were carried out by I. S., D.H, and J. G. Majority of the measurement code was written by V. V. and J. G. Furthermore, J. Y. T. and K. W. C. fabricated the sample of Supplementary Note I that was measured and analyzed by M. P. and K. Y. T. The sample in Supplementary Note II was produced by R. E. L. and A. L., and measured mostly by J. G. The manuscript was written by R. K., J.-P. G., and M. M. with the help of comments from all authors. The work was actively supervised by P. H. and M. M.

Other publications by the author

[Partanen2019] M. Partanen, J. Goetz, K. Y. Tan, K. Kohvakka, V. Sevriuk, R. E. Lake, R. Kokkoniemi, J. Ikonen, D. Hazra, A. Mäkinen, E. Hyyppä, L. Grönberg, V. Vesterinen, M. Silveri, and M. Möttönen. Exceptional points in tunable superconducting resonators. *Physical Review B*, **100**, 134505, October 2019.

[Kokkoniemi2017fatique] R. Kokkoniemi, A. Miksic, M. Ovaska, L. Laurson, M. J. Alava. Intermittent crack growth in fatigue. *Journal of Statistical Mechanics: Theory and Experiment*, **2017**, 073401, July 2017.

1. Introduction

Bolometry is one of the oldest forms of radiation sensing techniques. It relies on the fact that if material absorbs additional energy in any form of radiation, the temperature of the material increases. The power of the radiation can thus be measured indirectly by measuring the rise in temperature. The earliest bolometer was conceived by S. Langley back in 1880 [1]. The material absorbing the radiation in Langley's bolometer was thin strips of metal arranged in Wheatstone configuration. The radiation incident on one of the metal strips changes its temperature, and thus, the resistance. If a battery is connected across the Wheatstone bridge, the change in temperature can be read with a sensitive galvanometer measuring the difference of currents passing through the two arms. The Langley's bolometer was sensitive enough to detect the main Fraunhofer lines.

Key scientific discovery advancing bolometry further was the observation of superconductivity in the early 1900s [2]. It was noticed that if mercury is cooled to sufficiently low temperatures, its ability to resist the flow of electrical current suddenly vanished, i.e., electrical current can flow in a loop of superconductor indefinitely. A few decades after the discovery of superconductivity this sharp drop in resistance gave rise to a bolometer type referred to as a transition edge sensor (TES). However, the low resistance and extremely sharp drop of resistance with temperature made it at first unstable and difficult to operate.

Another important discovery made in the 1960s was the invention of the so-called Josephson junction [3]. Such a junction is formed by connecting two superconductors through a link where superconductivity is weakened such as a thin insulation layer, normal metal, or constriction in the superconductor. We explore the properties of superconductor–normal-metal–superconductor (SNS) Josephson junctions in Publication I. Josephson junctions have the remarkable property that electrically they behave as non-linear inductors. This non-linearity, along with many other properties, renders the Josephson junction a fundamental building block for circuit quantum electrodynamics (cQED), similarly what p-n junctions are for

regular electronics.

Quantum bit, or qubit, is one of the most interesting applications for Josephson junctions [4–6]. Many qubits operating in a coherent manner may realize a quantum computer [7], a computational device that promises superior performance over classical computer in certain tasks [8–10]. Quantum computers are still in their early development phase. The current record of qubits on a single chip is around 50 [11]. As the number of qubits is increased, it becomes more and more difficult to fit all cabling and off-chip components into a cryostat needed for qubit control and readout. Furthermore, the number of required room temperature instruments scales up with the number of qubits. Therefore, it is highly desirable to move as much of the instruments as possible into the cryostat and even into the quantum-processor package itself. Recent years have witnessed progress towards this goal with introduction of on-chip microwave attenuator [12], modulator [13], switch [14], gyrator [15], circulator [16], coherent microwave source [17], single-photon sources [18–20], and single-photon detectors [21–31]. This list is by no means exhaustive but exemplifies the great effort put towards miniaturizing the required instruments and components. In Publications II and III, we utilize Josephson junctions to create a magnetic-flux-tunable phase shifter. Such a device could be used, for example, in conjunction with an on-chip microwave source to move bulky room-temperature signal generators into the cryogenic environment.

The core of this thesis focuses on bolometry. This over a century old technology still remains in use today due to its flexibility in terms of the center frequency, bandwidth, and dynamic range. Bolometers are widely applied, for example, in gas detection [32], security [33], THz imaging [34], astrophysical observations [35], and medical applications [36]. Problems of early TESs have since been solved [37, 38] and are arguably today the most mature thermal detection technology. Thus, they are often employed in astronomical observation in both ground [39] and space-based observatories [40, 41] which require high technological readiness level. Interestingly, bolometers have recently emerged as candidate for detection of hypothetical dark matter particles [42–45].

In quantum technology, a bolometer could be used for the characterization of cryogenic environments, cabling, and various microwave components at a single-photon power level. Advancing bolometers into the single-microwave-photon regime would enable their their application in many experiments such as quantum illumination [46, 47], entanglement generation [48], parity measurement [49], and direct qubit readout [50, 51]. Possibility to frequency-multiplex bolometer readout could prove useful in large scale quantum computers since many qubits operating at the same carrier frequency could be read out with an array of bolometers.

Radiation detectors are often characterized in terms of noise equivalent power (NEP) which quantifies the noise in the readout signal in the units

of input power. State of the art thermal detectors, such as transition-edge sensors, have reached NEP of 300 zW/$\sqrt{\text{Hz}}$ in the far-infrared regime [52]. Alternative concepts, such as kinetic inductance detectors have reported similar sensitivities [53]. Far more promising NEPs below 10 zW/$\sqrt{\text{Hz}}$ have been measured from qubit-based quantum-capacitance sensors [54]. Semiconducting charge sensors [55] are expected to have an even lower NEP, but the full characterization is lacking.

Very few cryogenic bolometers have targeted the microwave regime [56, 57]. Calorimeters have recently reached the limit of fundamental temperature fluctuations in thermometry, promising the possibility of detecting single microwave photons [58]. Qubit based single-photon detectors have already demonstrated the ability to detect single propagating photons in microwave frequencies. However, they suffer from narrow bandwidth, typically of the order of 10 MHz, and dynamic range is limited to a single [31, 59, 60] or a few photons [61].

In Publication IV, we characterize an SNS-junction-based bolometer. We connect capacitors in parallel with the SNS junction, thus forming an LC oscillator. The resonance frequency of the oscillator becomes temperature dependent, due to strong temperature dependency of the inductance of the SNS junction, thus the resonance frequency acts as our thermometer. The normal-metal section of the junctions is connected to a 50-Ω resistor acting as an absorber of microwave radiation. The absorber and thermometer are thermally coupled in our design, but electrically isolated. This allows the readout and detection frequencies to be independent. Thus, we employ a relatively high readout frequency of about 0.5 GHz. In this initial study, we limit the detection frequency to 8.4 GHz with a bandpass filter.

We show in Publication IV that sensitivity of our bolometer surpasses the state of the art TESs [40, 52, 62]. However, we are still far from the elusive single-photon limit at typical cQED frequency of about 10 GHz. This poses the question: how can we further increase the sensitivity? Trivial answer is to decrease the size of the absorbing element, which decreases the heat capacity, and therefore a smaller energy pulse causes a higher temperature increase in the sensing element. In our bolometer, the absorber width is about 120 nm, and the length is 1 μm. Fabrication techniques available today, allow decreasing the width down to roughly 20 nm, thus an order of magnitude improvement in performance is not inconceivable if the thickness is also decreased. However, we have a conflicting requirement that the absorber resistance should be close to 50 Ohms. The length of absorber would need to be decreased, but this would transform the absorber into an SNS junction which does not have purely a real impedance. An alternative way of improving the performance is to fabricate the absorber from material with lower heat capacity. A very tempting choice is to use two-dimensional materials, such as graphene, since they have significantly lower volume. Furthermore, extremely fast thermal time constant of 35

ps has been reported for a graphene-based bolometer [63] operating at a relatively high temperature of 5 K. Another recent study on graphene-Josephson-junction-based bolometer predicted an NEP of 700 zW/$\sqrt{\text{Hz}}$ and energy resolution down to $h \times 32$ GHz at 0.19 K. However, the time constant was not experimentally determined, thus results need to be verified in practice.

In Publication V, we demonstrate a bolometer based on a superconductor–graphene–superconductor junction, the operation principle of which similar to the bolometer studied in Publication IV. We measure a low NEP of 30 zW/$\sqrt{\text{Hz}}$ together with a time constant of 500 ns. These results indicate an energy resolution of $h \times 30$ GHz, thus showing that bolometers are finally operating at the threshold for cQED, starting from the qubit readout application where a few photons in the 10-GHz range are typically used.

This thesis is organized as follows: Chapter 2 provides a brief theoretical background of basic principles employed in each publication. We start from the theoretical description of Josephson junctions, how their microwave admittance can be measured, and how they can be used in constructing a phase shifter. We finish this chapter by discussing the operation principles of thermal detectors. In chapter 3, we describe the measurement schemes used in this thesis. Chapter 4 summarizes the findings of Publication I where we measure the admittance of SNS Josephson junction. In Chapter 3, we discuss the experimental and theoretical results of Publications II and III which introduced and demonstrated wide-band operation of flux-tunable phase shifter, respectively. In Chapter 6, we go over the main results of Publications IV and V. Chapter 7 summarizes this thesis and provides possible paths for further refining the findings of this thesis.

2. Theoretical background

In this chapter, we provide a brief overview of the theoretical background and measurement methods relevant to publications presented in this thesis. In Sec. 2.1, we discuss Josephson junctions. We explain how to measure the impedance of such junction in Sec. 2.2. Section 2.3 shows theoretically how a phase shifter can be constructed with Josephson junctions. We conclude this chapter with a brief review of the fundamentals of thermal detectors in Sec. 2.4.

2.1 Josephson junction

The Josephson junction is a central element in all of the publications presented in this thesis. This stems from the fact that Josephson junctions behave electrically as inductive elements. In Publication I, we experimentally measure this inductance. Publication II shows how a tunable phase shifter can be constructed out of inductors. Josephson junctions also turn out to be a prime candidate for thermometry, since its inductance can be made strongly temperature dependent. We exploit this property in Publications IV and V.

A Josephson junction is formed by connecting two superconductors with a weak link. This weak link can be anything where superconductivity is

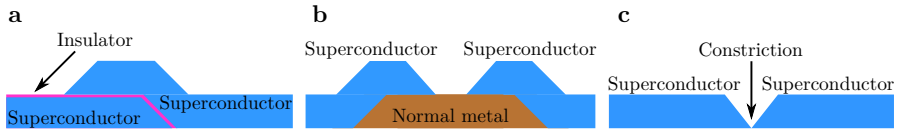

Figure 2.1. Examples of different types of Josephson junctions. **a**, In superconductor–insulator–superconductor Josephson junction, the two superconductors (light blue) are separated by a thin insulating layer (pink). Typically the thickness of the insulator is a few nanometers. **b**, Superconductor–normal-metal–superconductor Josephson Junction. Here, the two superconductors are separated by and galvanically connected to a section of normal metal. **c**, In superconductor–constriction–superconductor Josephson junction, suppression of superconductivity is realized by fabricating a constriction into the superconducting leads.

suppressed, such as a thin insulator layer or a short section of normal metal. A few examples of schematic cross-sections of different types of junctions are shown in Fig. 2.1.

Josephson relations describe the current $I(t)$ flowing through the junction and voltage $V(t)$ across it. They are given by

$$I(t) = I_c \sin\left[\phi(t)\right], \tag{2.1}$$

and

$$\frac{\mathrm{d}\phi}{\mathrm{d}t} = \frac{2e}{\hbar} V(t), \tag{2.2}$$

where t is time, I_c is the critical current of the junction, i.e., the maximum supercurrent the junction can carry, ϕ is the phase difference of the superconducting wave function of the two superconductors, e is the elementary charge, and $\hbar = h/(2\pi)$ is the reduced Planck's constant. Taking time derivative of Eq. (2.1) and substituting Eq. (2.2) to the result yields

$$V(t) = \frac{\hbar}{2eI_c \cos\left[\phi(t)\right]} \frac{\mathrm{d}I}{\mathrm{d}t}. \tag{2.3}$$

The above equation is identical to the current-voltage relation of an inductor. Thus, a Josephson junction behave as a non-linear inductor with inductance of $\hbar / \left\{2eI_c \cos\left[\phi(t)\right]\right\}$. The nonlinearity arises from the fact that the superconducting phase difference ϕ depends on the current flowing through the junction. This behavior of the Josephson junction as an inductor is what forms the basis of superconducting electronics and the non-linearity allows the realization of artificial atoms [64].

The Josephson junction can be used as a thermometer in thermal detectors since its critical current, and hence its inductance, is temperature dependent. However, for weakly coupled junctions, such as superconductor–insulator–superconductor (SIS) junctions, the critical current is almost independent of temperature at low temperatures [65]. At temperatures close to the critical temperature of the superconductor, the critical current becomes strongly temperature dependent and therefore can be used as a sensitive thermometer [66].

The situation is different for strongly coupled Josephson junctions, such as superconductor–normal-metal–superconductor (SNS) junctions. The critical current of an SNS junction exhibits strong temperature dependence down to a few percent of the critical temperature of the superconductor material [67]. Therefore, SNS junctions are a prime candidate for the thermometer in thermal detectors [68].

Transport properties of SNS junctions are often explained through the Usadel equation [69, 70]. However, since theory is not the core subject of this thesis, let us give here a qualitative explanation on the origin of the strong temperature dependency. Details of the Usadel equation can

be found, for example, from Ref. [71]. The charge carriers in superconductors are bound pairs of electrons. If such a pair is incident on the superconductor–normal-metal interface, it does not break instantly, but rather propagates some distance into the normal metal. Thus, the superconducting properties extend into the normal metal, which is called superconducting proximity effect [72]. The converse is also true, properties of the superconductor are weakened by the presence of the normal metal. Specifically, the normal metal can carry supercurrent while the critical current is diminished in the superconductor. The microscopic explanation of supercurrent in the normal metal is given by Andreev reflections [73]. For long junctions, the critical current suppression depends exponentially on the length of the normal metal and on the temperature [74]. Thus, the inductance of the junction changes exponentially with temperature, since the inductance is inversely proportional to the critical current.

An interesting effect arises if two Josephson junctions are connected in parallel such that they form a loop. The critical current of the junctions becomes highly sensitive to the magnetic flux threading the loop. Such an arrangement is referred to as a superconducting quantum interference device (SQUID). They are regularly employed in many applications where measurement of weak magnetic fields are needed [75]. In bolometry, SQUIDs are used as current amplifiers [76] especially for transition edge sensors [38, 77].

The inductance of a SQUID is given by

$$L_{\mathrm{SQUID}} = \frac{\Phi_0}{4\pi I_c \cos(\Phi_{\mathrm{ext}}/\Phi_0)}, \tag{2.4}$$

where $\Phi_0 = h/(2e)$ is the magnetic flux quantum, and Φ_{ext} is the external flux threading the SQUID loop. Therefore, a SQUID can be modeled as a flux-tunable inductor.

2.2 Admittance of SNS junctions

The problem with the Usadel equations is that sparse experimental data for the admittance of SNS junctions makes it difficult to validate the theory at microwave frequencies. Due to lack of well tested theory, fabrication of SNS junctions with desired properties requires trial and error. One way of measuring the admittance is to ground a resonator through the junction. This makes the resonance frequency and the quality factor to depend on the admittance of the junction. If we model the junction as a parallel connection of an inductor and a resistor, we can map the resonance frequency and the quality factor to the resistance and inductance of such circuit. Let us derive the equation which maps these quantities to each other.

Voltage $V_n(x,t)$ and current $I_n(x,t)$ in the resonator at position x and time t for each resonator mode n obey the Telegrapher's equations [78]. Thus, they can be written as a sum of left and right propagating waves given by

$$V_n(x,t) = N_n \left[e^{i(k_n x + \alpha_n t)} + A_n e^{-i(k_n x - \alpha_n t)} \right], \tag{2.5}$$

and

$$I_n(x,t) = \frac{1}{Z_0} N_n \left[-e^{i(k_n x + \alpha_n t)} + A_n e^{-i(k_n x + \alpha_n t)} \right], \tag{2.6}$$

where $k_n = \alpha_n / v$ is wave number for a wave with velocity v, $\alpha_n = \omega_n + i\gamma_n$ is the complex angular frequency of the wave, Z_0 is the characteristic impedance of the resonator, and A_n and N_n are complex coefficients determined by the boundary conditions. Note, that the above two equations are complex valued in order to make the following calculations simpler. Measured values can be obtained by taking the real part of the above two equations. Assuming that the energy deposited into the resonator decays exponentially, the complex resonance frequency is related to the quality factor Q_n of the resonance by $Q_n = \omega_n / (2\gamma_n)$. The voltage and current can be Fourier transformed as

$$\tilde{V}_n(x,\omega) = N_n \left[e^{ik_n x} \delta(\omega - \alpha_n) + A_n e^{-ik_n x} \delta(\omega - \alpha_n) \right], \tag{2.7}$$

and

$$\tilde{I}_n(x,\omega) = \frac{N_n}{Z_0} \left[e^{ik_n x} \delta(\omega - \alpha_n) - A_n e^{-ik_n x} \delta(\omega - \alpha_n) \right]. \tag{2.8}$$

In practice, the resonator is coupled to the external measurement circuit through a capacitor. Let us choose the coordinate system such that the coupling capacitor is at position $x = 0$, and the terminating junction is at position $x = l$. The physical size of these components is small compared to the length l of the resonators, thus they can be modeled as point-like objects. The boundary conditions for current and voltage with this choice read

$$-\tilde{I}(0,\omega) = \frac{\tilde{V}(0,\omega)}{Z_{\text{coup}}}, \tag{2.9}$$

and

$$\tilde{I}(l,\omega) = \frac{\tilde{V}(l,\omega)}{Z_{\text{term}}}, \tag{2.10}$$

where Z_{coup} is the impedance of the coupling capacitor, and Z_{term} is the impedance of the termination junction. The minus sign in the first equation above takes into account the positive direction of the current. Insertion of Eqs. (2.7), and (2.8) into Eq. (2.9) yields

$$A_n = \frac{Z_{\text{coup}} - Z_0}{Z_{\text{coup}} + Z_0}. \tag{2.11}$$

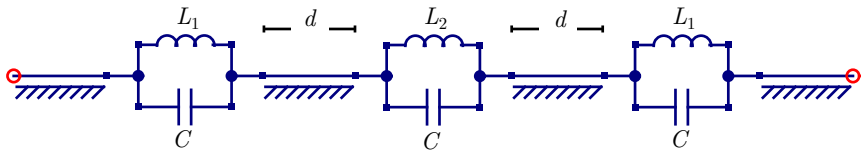

Figure 2.2. Lumped-element model of the phase shifter. The phase shifter consists of three equidistant SQUIDs which are modeled as parallel LC oscillators. The inductors at far ends have an inductance of L_1 and the inductor in the middle has an inductance of L_2. All SQUIDs are modeled to have equal capacitance C. The LC oscillators are separated by transmission lines of length d. The figure is adapted from Publication II.

Since the coupling is purely reactive, we can write the above equation as

$$A_n = -e^{-i2\arctan(\mathrm{Im}[Z_{\mathrm{coup}}]/Z_0)}. \tag{2.12}$$

Similarly, Eqs. (2.7), (2.8) and (2.10) lead to

$$\frac{e^{ik_n l} - A_n e^{-ik_n l}}{e^{ik_n l} + A_n e^{-ik_n l}} = -\frac{Z_0}{Z_{\mathrm{term}}}. \tag{2.13}$$

Substitution of Eq. (2.12) into Eq. (2.13) yields

$$i\tan\left[\frac{\omega_n}{2f_0}\left(1+\frac{i}{2Q_n}\right)+\arctan\left(Z_0\omega_n C_{\mathrm{coup}}\right)\right] = -\frac{Z_0}{Z_{\mathrm{term}}}, \tag{2.14}$$

where $f_0 = v/(2l)$ is the bare resonance frequency of the resonator. With the above equation, we can map the measured resonance frequencies and quality factors to the unknown resistances and inductances.

2.3 Phase shifter

An interesting phenomenon appears if we interrupt a transmission line with three equidistant inductors, such that the middle inductor has inductance L_2, and the two others have equal inductance L_1. Such a system may exhibit unit transmission coefficient magnitude, but the phase depends on the inductances and on the signal frequency. Thus, if the inductors are SQUIDs, we can use this configuration as a flux-tunable phase shifter. Note that three is the minimum number of SQUIDs needed to construct a phase shifter. We need two parameters to set the reflections to zero and tune the phase of the transmitted signal. Since phase shifter is symmetric, two SQUIDs would yield only one free parameter, thus we need at least three SQUIDs.

If the SQUIDs are fabricated with SIS-type Josephson junctions, they have significant parallel capacitances, which is straightforward to include in our model shown in Fig. 2.2. Derivation of transmission coefficient in the

context of circuit quantum electrodynamics is given in the supplementary material of Publication II. Let us take here an alternative approach employing the so-called ABCD-parameter method [79] as an instructive exercise. For a two-port system, the ABCD-matrix relates the input voltage and current to the output output voltage and current. Each component of the system is described as a 2-by-2 matrix in this method. ABCD-parameters for a transmission line are given by

$$\mathbf{T} = \begin{bmatrix} \cosh(i\phi) & Z_0 \sinh(i\phi) \\ \sinh(i\phi)/Z_0 & \cosh(i\phi) \end{bmatrix}, \tag{2.15}$$

where $\phi = \omega d/v$ is the phase shift due to superconducting transmission line of length d, with wave velocity v at signal angular frequency ω, and Z_0 is the characteristic impedance of the transmission line. The parameters for the middle ($\mathbf{M}_1$) and side ($\mathbf{M}_2$) SQUIDs can be written as

$$\mathbf{M}_i = \begin{bmatrix} 1 & Z_i \\ 0 & 1 \end{bmatrix}, \tag{2.16}$$

where $Z_i = \left[(i\omega L_i)^{-1} + i\omega C\right]^{-1}$ is the impedance of the side ($i = 1$) or middle ($i = 2$) SQUID with parallel capacitance C. The ABCD-parameters of the full system $\mathbf{F}$ are obtained by multiplying together the matrices in order they appear in the system, i.e., $\mathbf{F} = \mathbf{M}_1\mathbf{T}\mathbf{M}_2\mathbf{T}\mathbf{M}_1$. The transmission coefficient is given by $S_{21} = 2\left(\mathbf{F}_{1,1} + \mathbf{F}_{1,2}/Z0 + \mathbf{F}_{2,1}Z_0 + \mathbf{F}_{2,2}\right)^{-1}$, where $\mathbf{F}_{i,j}$ is the element of matrix $\mathbf{F}$ on ith row and jth column. This yields

$$S_{21} = \frac{2Z_0 X f(0)\left(CL_1\omega^2 - 1\right)\left[2Z_0\left(CL_1\omega^2 - 1\right) + iL_1\omega f(-1)\right]^{-1}}{X - 2i\omega Z_0\left[CL_1L_2\omega^2 f(2) - L_2 - L_1 f(1)\right] + L_1L_2\omega^2 f(-1)}, \tag{2.17}$$

where $X = 4Z_0^2\left(CL_1\omega^2 - 1\right)\left(CL_2\omega^2 - 1\right)$, and $f(x) = e^{-2i\phi} + x$.

Let us define a free real parameter θ, and parametrize the inductances L_1 and L_2 as

$$L_1 = \frac{2Z_0 \sin(\theta/2)}{\omega\left[2C\omega Z_0 \sin(\theta/2) + \cos\left(\theta/2 - 2\phi\right) - \cos(\theta/2)\right]}, \tag{2.18}$$

and

$$L_2 = \frac{4Z_0 \sin(\theta/2)\cos\left(\theta/2 - 2\phi\right)}{\omega\{2C\omega Z_0\left[\sin(\theta - 2\phi) + \sin(2\phi)\right] - \cos(2\phi) + 1\}}. \tag{2.19}$$

Substituting the above ansatzes to the Eq. (2.17) yields

$$S_{21} = e^{-i(2\phi - \theta)}. \tag{2.20}$$

Thus, a transmission line interrupted by three equidistant SQUIDs does indeed behave as a tunable phase shifter with phase tunability of θ. It is

not immediately obvious if there exists such combination of θ and ω that Eqs. (2.18) and (2.19) would result in realistic inductance. We attempt to answer this question in Sec. 5.

2.4 Thermal detectors

All thermal detectors have three elements in common: an absorber that absorbs the incident radiation, a thermal link connecting the absorber to a thermal bath, and a temperature sensor for measuring the temperature of the absorber. Figure 2.3 shows a schematic drawing of a thermal detector and its different operation modes. If continuous radiation is absorbed by the detector, its temperature T increases by an amount determined by the power of the radiation P_{h} and by the thermal conductance G between the absorber and the thermal bath. Thus, the incident radiation power can be determined indirectly by measuring the increase in the temperature of the absorber. The temperature increases exponentially towards the final value with the time constant τ set by the heat capacity C and the thermal conductance of the absorber as $\tau = C/G$. A thermal detector used for measuring the power of continuous radiation is called a bolometer. Another important quantity of thermal detectors is the increase of temperature per unit input power, or responsivity. Note that very rarely, bolometers measure temperature directly. They usually measure either current or voltage, which is made temperature dependent through some physical process. For example, if a constant current is driven through a temperature-dependent resistor, the voltage measured across the same resistor is also temperature dependent. The voltage can be calibrated to read out temperature using a separate thermometer. However, this is rarely done in bolometry, since only relative differences in temperature are needed to determine the input power.

A sensitive and fast bolometer can also be used to detect single particles or pulses of radiation at much shorter time scales than the thermal time constant. The increase of temperature in such single-particle detection is determined by the energy of the absorbed particle, or pulse of radiation, and by the heat capacity of the absorber. A thermal detector used for single-particle detection is also referred to as a calorimeter.

The bolometric mode of operation is often characterized in terms of noise equivalent power (NEP). In this thesis, we take the definition of the NEP to be the noise density of the bolometer output expressed in units of the input power. The NEP quantifies the power that can be detected with unit signal to noise ratio in 1/2 second of integration time. In practice, the NEP is measured by measuring the noise density of the bolometer output, which is further divided by the responsivity.

The figure of merit for the calorimetric mode is the energy resolution

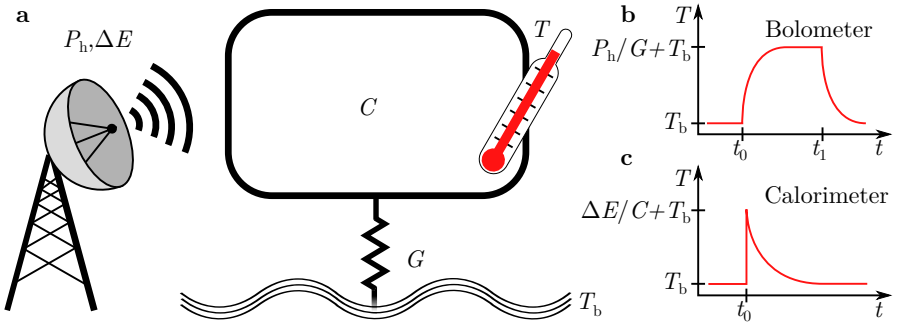

Figure 2.3. Simplified operation principle of thermal detectors. **a**, Typical elements of thermal detectors. Absorber with heat capacity C is connected to a thermal bath at temperature T_b through a link with thermal conductance G. The radiation incident on the absorber increases its temperature T, which is measured with a thermometer. **b** Bolometric mode of operation. If constant heating power P_h is turned on at time $t = t_0$, it increases the absorber temperature exponentially to a final value of $P_h/G + T_b$ with time constant $\tau = C/G$. Similarly, if the heating power is turned off at time $t = t_1$, the temperature of absorber decreases exponentially back to the bath temperature. **c** Calorimetric mode of operation. If a short pulse with energy ΔE is absorbed by the calorimeter, its temperature rises fast to temperature $\Delta E/C + T_b$. The temperature begins to drop exponentially back to the equilibrium value immediately after the absorption event.

ΔE, which simply equals the smallest detectable energy packet with unit signal-to-noise ratio. A fundamental result of statistical physics is that the energy of an object in thermal equilibrium with its environment at temperature T will fluctuate with mean square value of $\overline{\delta E^2} = k_B T^2 C$. The energy fluctuation is often quoted as the fundamental bound of energy resolution due to thermal fluctuations. The same fluctuations also impose a lower bound for the NEP given by [80] $\mathrm{NEP_{TFN}} = \sqrt{4k_B T^2 G}$. It is therefore evident, that both thermal conductance and heat capacity of the absorber should be made as small as possible in order to achieve a sensitive and fast thermal detector. However, thermal fluctuations may occur at low frequencies, thus they do not necessarily impose a strict bound on the NEP or the energy resolution.

Other major noise contributions are the shot noise and readout amplification chain noise. The shot noise arises from the random nature of photons being absorbed by the detector. This is proportional to the square root of the signal power used to read out the bolometer. The amplification of the readout signal also adds a significant amount of noise. Therefore, careful engineering of the readout path is necessary. We take a closer look at this in Chapter 3.

3. Measurement scheme

In this chapter we explain the general principles of the measurement setups employed in this thesis. All measurements presented in this thesis employ signal powers well below the room temperature thermal noise level. Therefore, it is of utmost importance to carefully engineer the electromagnetic environment of the samples. As a general rule, all signal input lines reaching the sample must be sufficiently attenuated and limited in bandwidth in order to suppress the thermal noise. The output signal lines cannot be attenuated, otherwise any signal coming out of the samples would be lost. Therefore, the bandwidth of output lines should be limited as much as reasonable. In addition, a device referred to as an isolator should be placed on the output line. It allows the signal to pass only in one direction, thus preventing thermal radiation and amplifier noise from reaching the sample. Below, we discuss the different measurement setups used in publications presented in this thesis.

3.1 Phase shifter and admittance of SNS junctions

In Publications I, II, and III, the measurement setup is rather simple since only frequency domain information is needed. This requires only two rf lines, one for input and one for output. The input line has attenuators on each temperature stage for two reasons: firstly, they thermally anchor the rf line to the different temperature stages, and secondly, they attenuate the thermal radiation originating from higher temperatures. The attenuators also reduce the signal power to low enough level where the Josephson junctions can be modeled as linear inductors.

The output rf line in experiments of Publication II has two isolators with a passband of 4 to 8 GHz protecting the sample from amplifier noise. This is not possible in experiments of Publication I due to the wide frequency range of the measurement. The higher noise level is counteracted by simply using longer averaging times.

Measurements in both publications are carried out with a vector network

analyzer (VNA) which directly measures the complex transmission coefficient. In Publication II, we need an additional three current bias lines to create a local magnetic field for each SQUID. In contrast, experiments of Publication I require only a global magnetic field, which is produced by a coil placed outside of the sample holder. Since the samples in both of these publications are sensitive to magnetic fields, they are placed inside a magnetic shield preventing external magnetic fields from disturbing the measurements.

3.2 Bolometry

The bolometer measurements require time-domain information in addition to the frequency domain. Therefore, the measurement setup becomes slightly more complicated. In addition, the bolometers are by definition sensitive to temperature, thus the electromagnetic environment must be engineered very carefully to limit excess thermal radiation entering the sample. The detailed measurement setup for a typical bolometer experiment is shown in Fig. 3.1. Let us discuss how the different parts of the setup allow reaching the above requirements.

3.2.1 Low temperature setup

Let us first focus on the setup inside the cryostat. The leftmost rf line in Fig. 3.1 is used to apply microwave heating to the bolometer sample. This is a simple heavily attenuated coaxial cable. The heater bandwidth is limited by the on-chip coplanar waveguide (CPW) resonator, which has a passband of about 50 MHz centered at 8.5 GHz. A Thermocoax-cable is used to prevent radiation at harmonics of the CPW resonator from entering the sample, since attenuation of the Thermocoax cable increases exponentially with frequency [81].

The second line from the left in Fig. 3.1 is the probe input line. This is otherwise nearly identical to the heater line, except that the signal is taken to the sample through extra filtering and a directional coupler. The coupler adds another 20 dB attenuation to the input line, but the signal reflected from the sample goes through it with minimal loss. The directional coupler could be replaced with a circulator. However, the directional coupler has several advantages. Firstly, the insertion loss of a directional coupler is typically lower than that of a circulator. Secondly, circulators for the probe frequencies employed are bulky and custom made, thus, expensive. Thirdly, a directional coupler provides much higher isolation of probe input and output signal compared with a circulator, i.e. almost none of the probe input signal goes directly to the output bypassing the sample.

The third rf line in the cryostat is the probe output line. Here, we use

filters and isolators to reduce the thermal radiation reaching the sample. The signal is amplified with a high-electron-mobility-transistor (HEMT) amplifier placed at the 4-K stage. The main advantage of low-temperature amplifiers is that they add significantly lower amount of noise to the signal when compared to the room temperature amplifiers. We also have an option to add a Josephson parametric amplifier (JPA) [82] to the amplification chain. The main advantage a JPA is that it adds an order of magnitude less noise to the signal than regular HEMT amplifiers. This comes at the cost of more complex measurement procedure due to required dc-bias and pump tone which need to be readjusted every time probe frequency changes.

The final point of consideration in the cryogenic setup is shielding from external thermal radiation. The cryostat walls are at finite temperature, thus they emit thermal radiation. In order to protect the sample from this radiation, we place it in a small sample holder which is made out of gold-plated copper. This small sample holder is further enclosed in a larger gold-plated copper box which is bolted to the coldest stage of the cryostat. Therefore, the environmental thermal radiation entering the sample is significantly reduced.

3.2.2 Room temperature setup

Let us move discuss the room temperature setup. The heater line is otherwise just a plain coaxial cable, but there is an attenuator at the input of the cryostat to reduce the power entering the cryostat. The probe input line has also a directional coupler in addition to an attenuator. The directional coupler is used to take a copy of the probe signal. This copy is used as a phase reference in frequency domain measurements. The copied signal is downconverted to 70.3125 MHz with a mixer. The downconverted reference signal is amplified and bandpass filtered before digitization.

The probe output signal is further filtered and amplified at room temperature with three stages of amplification. We place 3-dB attenuators between the amplifiers in order to reduce possible standing waves between amplifiers and filters. The probe output signal is similarly downconverted, amplified, and bandpass filtered as the reference signal. The local oscillator is split into the two mixers with a reactive power splitter. The local oscillator frequency is related to the probe frequency by $f_{\mathrm{LO}} = f_{\mathrm{p}} - 70.3125$ MHz.

Both the reference signal and probe signal are digitized after downconversion with a 14-bit analog-to-digital converter (ADC) connected to a field-programmable gate array (FPGA) board. Three major data collection tasks are carried out on the FPGA. First, the 70.3125 MHz signal is digitally converted down to dc, thus we obtain amplitude and phase of the probe signal as a function of time. Next, we sum together every second sample with its neighbor due to technical reasons. We also have an option

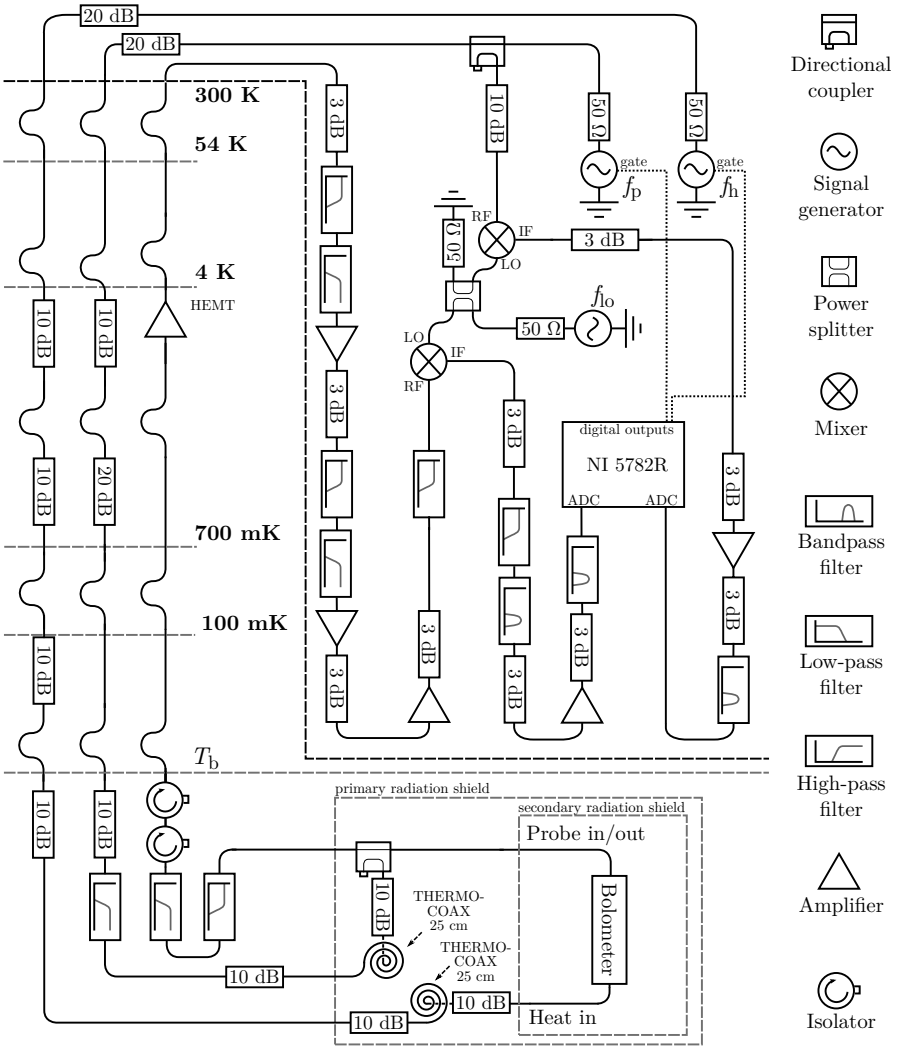

Figure 3.1. Typical measurement setup for a bolometer. Different temperature stages are marked with dashed lines. Bends in the rf lines denote extra length of the cable thermally isolating the temperature stages. The meaning of different symbols are defined on the right hand side of the schematic.

to sum more than two samples if we wish to make long measurements without collecting huge amounts of data. Finally, the FPGA has the capability of ensemble averaging, i.e., after collecting a predetermined number of data points, the FPGA repeats an identical measurement for a desired amount of times and takes the average of all measurements. This averaged data is transferred to a computer for further data processing. In addition, the FPGA also turns on and off the probe and heating signals at correct times.

4. Admittance of SNS Josephson junction

Response of SNS Josephson junctions to direct current is well understood theoretically and thoroughly tested experimentally [67, 69, 83–86]. However, there are plenty of open questions in the microwave response of the junctions. Although theoretical models exist [70, 87–90], experimental data to verify the models is sparse [91, 92]. In this chapter, we summarize the findings of Publication I where we present a method to quantitatively determine admittance of an SNS junction.

4.1 Measurement of unknown admittance

As discussed in Sec. 2.2, the admittance of an SNS junction can be determined from the resonance frequency and quality factor of a resonator grounded through the junction. To this end, we fabricate a multimode resonator capacitively coupled to a feedline. The other end of the resonator is grounded through capacitors and a chain of 20 SQUIDs as shown schematically in Fig. 4.1. We fabricate two nominally identical samples, 1 and 2, with the exception that Sample 1 does not have the heat sink fins shown in Fig. 4.1c. Replacing the single junction with a chain of SQUIDs brings the admittance to more conveniently measurable range, but also adds an additional degree of freedom to the measurement. However, we can still find the mean admittance of a single junction by multiplying the total admittance by 10.

We parametrize the SQUID chain as a parallel connection of an inductor L and resistor R. Thus, the impedance of the termination is given by

$$Z_{\mathrm{term}} = (iC_{\mathrm{i}}\omega_n)^{-1} + \left(\frac{1}{iL\omega_n} + \frac{1}{R}\right)^{-1}, \tag{4.1}$$

where C_{i} is the capacitance of the coupling between the SQUID chain and the resonator. This capacitor is physically a parallel plate capacitor, and hence we can calculate its capacitance with good accuracy. The chain of SQUIDs is grounded through a large capacitor C_{gnd} which essentially acts

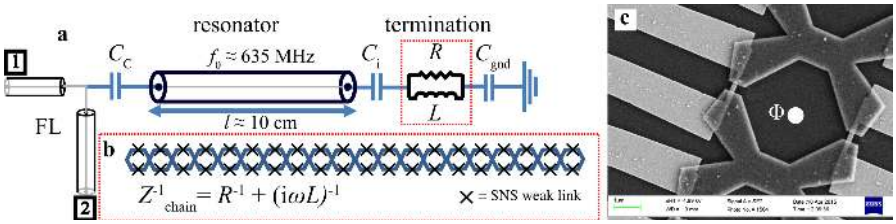

Figure 4.1. Measurement scheme for determining the admittance of SNS junctions. **a**, Electric-circuit model of the sample. The resonator of length $l = 10$ cm with fundamental resonance frequency of $f_0 \approx 635$ MHz is capacitively coupled to a feedline (FL). The other end of the resonator is capacitively coupled to a chain of SQUIDs shown schematically in panel **b**. The chain of SQUIDs is modeled as a parallel connection of a resistor and an inductor, which is grounded from the other end through a large capacitor. **c**, Scanning-electron-microscope image of a single SQUID. Light areas in the figure are gold-palladium forming, for example, the normal-metal sections of the SNS junctions. The purpose of the large rectangular regions is to keep the junctions well thermalized to the bath temperature. Darker cross-like shapes are made out of aluminum. Figure adapted from Publication I.

as a direct short to ground at the frequencies employed. Therefore, we can neglect its effect to the termination impedance.

The resonance frequencies and quality factors are extracted from the transmission coefficient S_{21}, measured through the feedline, as a function of frequency f. We fit a function to the normalized data given by [93, 94]

$$S_{21}(f) = 1 - \frac{\frac{Q_{0,n}}{Q_{C,n}} - 2iQ_{0,n}\frac{\delta f}{f_n}}{1 + 2iQ_{0,n}\frac{f - f_n}{f_n}}, \tag{4.2}$$

where $Q_{0,n}$ is the total quality factor, $Q_{C,n}$ is the quality factor arising from the coupling capacitor, $f_n = \omega_n/(2\pi)$ is the resonance frequency of mode n, and δf describes the asymmetry of the resonance. We are interested in the internal quality factor $Q_{i,n}^{-1} = Q_{0,n}^{-1} - Q_{C,n}^{-1}$ which arises from the internal losses in the resonator. Since the resonator is superconducting, the internal losses are dominated by the chain of SQUIDs. Once we have determined the resonance frequencies and quality factors as functions of the magnetic flux threading the SQUIDs, we map them to inductances and resistances with Eq. (2.14). We focus on the resonance near 1 GHz in the discussion below.

4.2 Discrepancy between theory and experimental results

We compare our experimental results to corresponding predictions of the time-dependent Usadel equations [70]. The temperature dependence of the inductance and resistance is in conflict with the theoretical calculations as show in Fig. 4.2. The low-temperature value of the single-junction inductance at $\Phi = 0$ flux point is found to be $L/10 \approx 300$ pH, which is almost an order of magnitude larger than the expected theoretical value of about

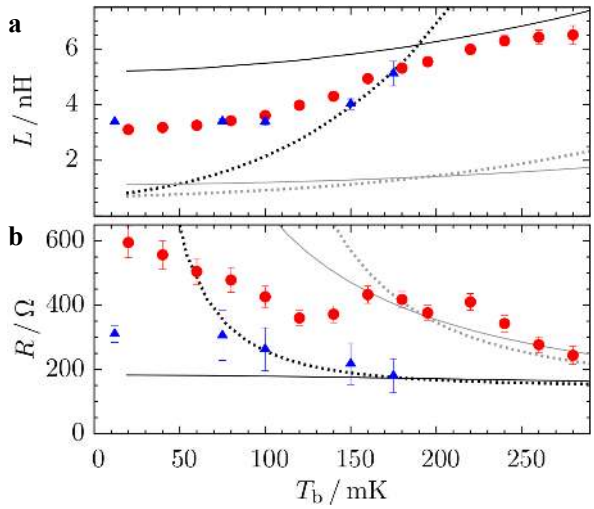

Figure 4.2. Temperature dependence of the inductance and resistance. **a**, **b**, Inductance (**a**) and resistance (**b**) of the SQUID chain as a function of bath temperature T_b for Sample 1 (solid blue triangles) and Sample 2 (solid red circles) at $\Phi = 0$ flux point. The dashed lines show theoretical values for high (black dashed line) and moderately high (grey dashed line) inelastic scattering rate. The solid lines show calculated values for strong (black solid line) and moderately strong (grey solid line) elastic spin-flip scattering. The spin-flip scattering calculations also include weak inelastic scattering. Figure adapted from Publication I.

50 pH. Furthermore, the expected exponential temperature dependence of the resistance at $\Phi = 0$ flux point is in stark contrast with observations.

We attempt to explain this difference by including inelastic scattering and spin-flip scattering in the theoretical model. The spin-flip scattering could arise if the normal-metal sections of the SQUIDs are contaminated with magnetic impurities. Note, that we do not know the exact origin of the scattering mechanisms. Thus, we do not know with certainty their temperature dependence. As an example, we choose that the inelastic scattering rate is proportional to the temperature, while the spin-flip scattering remains constant. In any case, it is clear that the observed resistance does not scale exponentially with the bath temperature and the theory does not coincide with the observations for the considered parameter ranges.

The measurement results for inductance and resistance as a function of the magnetic flux are shown in Fig. 4.3 along with theoretically calculated values. The experimentally determined inductance near integer flux quanta is in a reasonable agreement with the calculated values in the strong-scattering regime for both mechanisms. However, the strong scattering also decreases the variation of resistance with flux. Conversely, the theory is in good agreement with the measured resistance values for moderately strong scattering, whereas the inductance values differ significantly in this regime.

Our main conclusion of the Publication I is that if we were able to

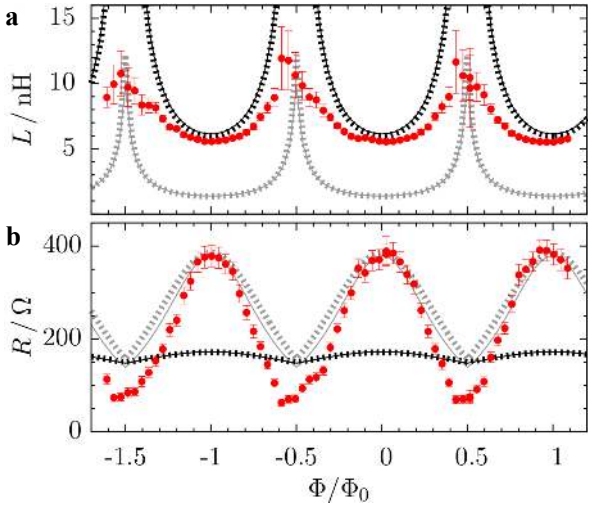

Figure 4.3. Magnetic-flux dependence of the resistance and inductance of SNS junctions. **a**, **b** Inductance (**a**) and resistance (**b**) of the SQUID chain as a function of magnetic flux Φ threading the SQUIDs for Sample 2. The solid and dashed lines are calculated from the theory with the same parameters as in Fig. 4.2. Here, the bath temperature is 195 mK. Figure adapted from Publication I.

measure only the inductance, we might make a false deduction that the theory matches with the observations. However, we are unable to find such parameters for the theoretical calculations that simultaneously reproduce the measured resistance and inductance. A possible explanation for this anomalous behavior is that magnetic effects are important to take into account in detail since palladium is known to become ferromagnetic in nanoscale systems [95, 96]. In the future, it may be constructive to study niobium-copper SNS junctions which have been shown to behave nearly ideally at dc [67, 97].

5. Flux-tunable phase shifter

In this chapter, we summarize the findings of Publication II, where we attempt to contribute to the quickly expanding quantum-engineering toolbox by introducing an on-chip flux-tunable microwave phase shifter. We demonstrate experimentally and theoretically its ability to tune the phase of a signal without losses or reflections.

5.1 The device and measurement setup

Our phase shifter consists of three equidistant SQUIDs interrupting a 50-Ω transmission line. We model each SQUID as a parallel LC oscillator. The Josephson junctions are of SIS type, which gives rise to the parallel capacitance. The device is shown in Fig. 5.1 along with the measurement scheme. As shown in Sec. 2.3, such a system exhibits full transmission while allowing the phase of the signal to be tuned.

The condition for achieving the full transmission is that the two side SQUIDs have an equal inductance L_1 and the middle SQUID has the inductance L_2. Assuming that the side SQUIDs have identical zero-flux critical current, the fluxes threading the two side SQUIDs must also coincide to Φ_1. The flux threading the middle SQUID is Φ_2. The capacitance C is assumed to be equal for all three SQUIDs.

The sample is cooled down to 13 mK in a commercial cryostat. The microwave transmission through the phase shifter is measured with a vector network analyzer with such a low power that the SQUIDs behave as linear inductors. The measured raw transmission coefficient includes the effect of all the components and cabling between the sample and the VNA. Therefore, it is necessary to normalize the transmission coefficient with a measurement for which we know that the effect of the SQUIDs is minimal. We choose this reference point to be such that all three SQUIDs are tuned to integer multiple of flux quanta. Here, the inductances of the SQUIDs are minimized, and thus the transmission through the phase shifter is sufficiently close to unity.

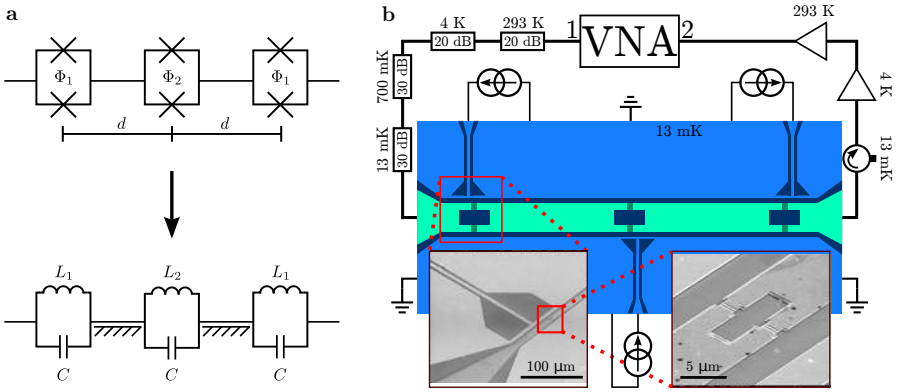

Figure 5.1. Model and measurement scheme of the phase shifter. **a**, Three equidistant SQUIDs are separated by transmission lines of length d. Flux threading the SQUIDs is denoted by Φ_k, the inductance by L_k, and capacitance by C. **b**, The transmission through the sample is measured with a vector network analyzer (VNA). The signal from the Port 1 of the VNA is guided to the phase shifter through heavily attenuated coaxial cables. The signal coming out of the sample is amplified with a low-temperature and room temperature amplifiers before arriving at Port 2 of the VNA. The sample is protected from the amplifier noise with an isolator. A local magnetic field for each SQUID is provided with the three current sources. Here, niobium is denoted with light blue color, aluminum with light green, Josephson junctions with dark green, and substrate with dark blue. The features are not drawn to scale. The insets show scanning electron microscope images of a single SQUID taken from a nominally identical sample to that measured. Figure adapted from Publication II.

5.2 Results

Figure 5.2 shows the measured normalized transmission coefficient along with the theoretical values at the signal frequency of 6.3 GHz. We observe near-unit transmission along the solid line in Fig. 5.2a–d where the transmission is theoretically exactly unity. Figure 5.2e shows the transmission coefficient along this line. We achieve phase shift tunability over $\pi/4$ radians with essentially vanishing losses. We attribute the small difference between theory and experiments to deviation from the assumption that the two side SQUIDs are identical.

We calculate the theoretically achievable phase tunability as a function of signal frequency by numerically solving from Eqs. (2.18) and (2.19) the phase shifts θ, for which the inductances are in a feasible range. The results shown in Fig. 5.3 indicate that large phase shifts can be achieved over a wide frequency ranges. However, there are certain frequency bands for which no realistic inductance values result in lossless transmission. These gaps fortunately depend on the distance d between the SQUIDs, thus it can be accounted for when designing a phase shifter for a certain frequency band. Note, that the sharp features in Fig. 5.3 arise from the limitations imposed on the inductance values, and hence are not numerical artefacts.

In order to experimentally verify the frequency dependency, we measure

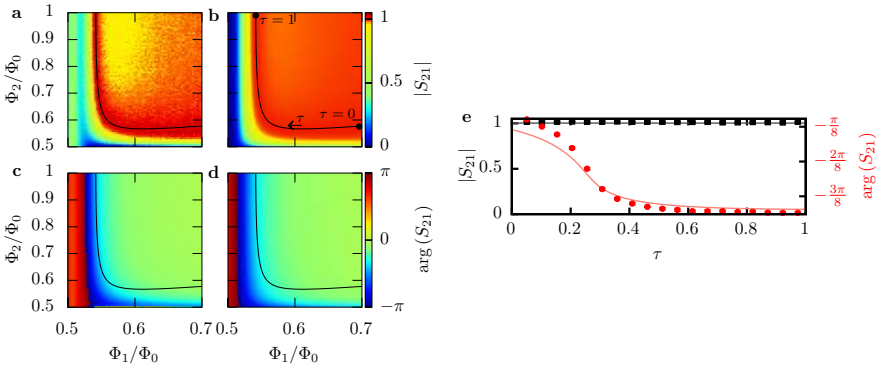

Figure 5.2. Measured and calculated transmission coefficients. **a**, **c**, Measured (**a**) magnitude and (**c**) phase of the transmission coefficient as a function of flux threading the side SQUIDs Φ_1 and middle SQUID Φ_2. **a**, **c**, As **a** and **c** but for the corresponding theoretical predictions. We define the parameter τ as the relative length along the theoretical full-transmission curve (solid line). The parameter vanishes at point ($\Phi_1 = 0.7$, $\Phi_2 \approx 0.58$) and is unity at point ($\Phi_1 \approx 0.54$, $\Phi_2 = 0.7$). **e**, The magnitude (black) and phase (red) of the measured (markers) and calculated (solid lines) transmission coefficient along the theoretical full-transmission curve. In the theoretical calculations, the zero-flux critical current of the two side SQUIDs is set to $I_{c,1} = 0.7$ μA, and $I_{c,2} = 2.2$ μA for the middle SQUID. The capacitance is $C = 26$ fF. Figure adapted from Publication II.

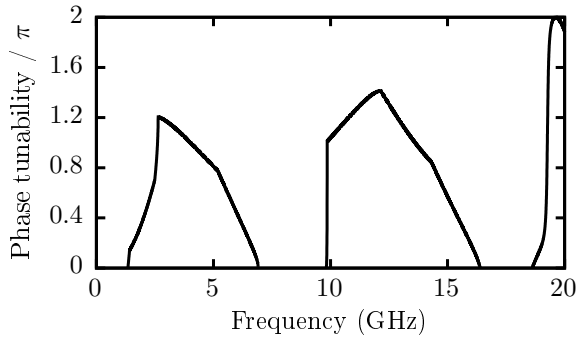

Figure 5.3. The calculated difference between the minimum and maximum phase shift achievable for inductances L_1 and L_2 such that their minimum value is larger than $\Phi_0/(4\pi I_{c,k})$, but less than 10 nH as a function of signal frequency. The minimum is set by inductance at integer flux quanta threading the SQUID, and the maximum is arbitrarily chosen value. Other parameters are the same as in Fig. 5.2. Figure adapted from Publication II.

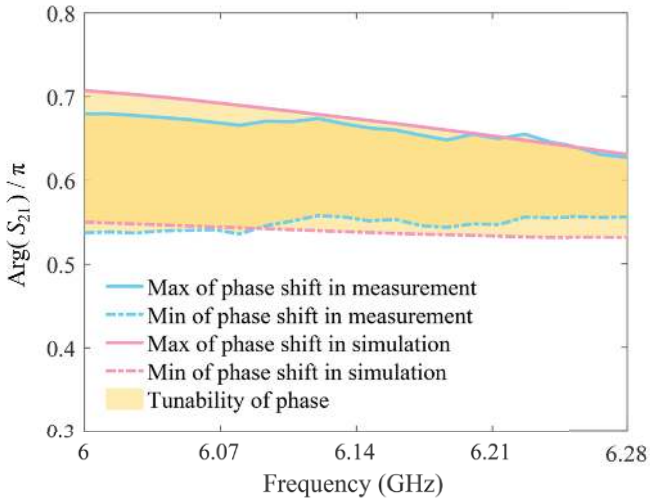

Figure 5.4. Maximum (solid lines) and minimum (dashed-dotted lines) phase shift obtained in experiments (blue color) and in circuit-simulations (red color) as functions of frequency. The shading defines the region of achievable phase shifts, i.e., the tunablity region of the phase shifter. Figure adapted from Publication III.

the tunability of the phase shift from a similar sample in Publication III. The sample is otherwise nominally identical to the sample measure in Publication II, except the flux bias lines were made differential. The measured phase tunability and corresponding simulation results are shown in Fig. 5.4. We find above 0.07π phase tunability over 280-MHz frequency band. Our measurement results are also in good agreement with phase shift simulated from an equivalent electric circuit.

Thus, we have experimentally and theoretically shown in Publications II and III that three equidistant SQUIDs interrupting a transmission line behaves as a tunable phase shifter with negligible losses. Interestingly, our calculations suggest that even a full 2π phase shift may be achievable for certain frequencies and parameter values. Our theoretical calculations also suggest that adding more SQUIDs to the system may realize larger phase shits than three-SQUID system.

6. Low noise bolometry with proximity junctions

This chapter provides perhaps the most impactful outcomes of this thesis. We summarize the main results of Publications IV and V, where we characterize gold-palladium and graphene-based bolometers, respectively.

6.1 Reaching record-low noise equivalent power

Let us first discuss the results of Publication IV. The absorber in the studied device is formed by a gold-palladium nanowire with the absorber resistance of 36 Ω. The central principle of our bolometer design is that this nanowire also defines the normal-metal parts of the eight thermometer SNS Josephson junctions connected in series. Therefore, these two parts of the bolometer are thermally strongly coupled. The junctions are grounded through capacitors C_1 and C_2 forming an LC oscillator as shown in Fig. 6.1a,b. The strongly temperature-dependent resonance frequency of the oscillator acts as our thermometer. The capacitor C_1 also electrically decouples the absorber and the SNS junctions.

Our choice of absorber material is a mixture of gold and palladium with a 2.5:1 atomic ratio. Small superconducting parts are made out of aluminum due to its compatibility with our highly mature fabrication techniques. This prevents using pure gold as a normal metal since aluminum and gold form intermetallic compounds, which will break the sub-micron scale structures over time. Adding palladium to the gold prevents this effect, and thus makes the bolometer stable.[1] Palladium is not an optimum choice due to its high specific heat capacity [98], but finding a better substitute would be worth another Ph.D. thesis, thus we leave such optimization for future work. Copper or silver might be interesting candidates since they both have an order of magnitude lower heat capacity than palladium.

The key feature making our bolometer noise low is that the change in the temperature is read out with a relatively high frequency of about 500 MHz.

[1] Some of the results presented in this thesis were obtained with samples fabricated two years before the measurements.

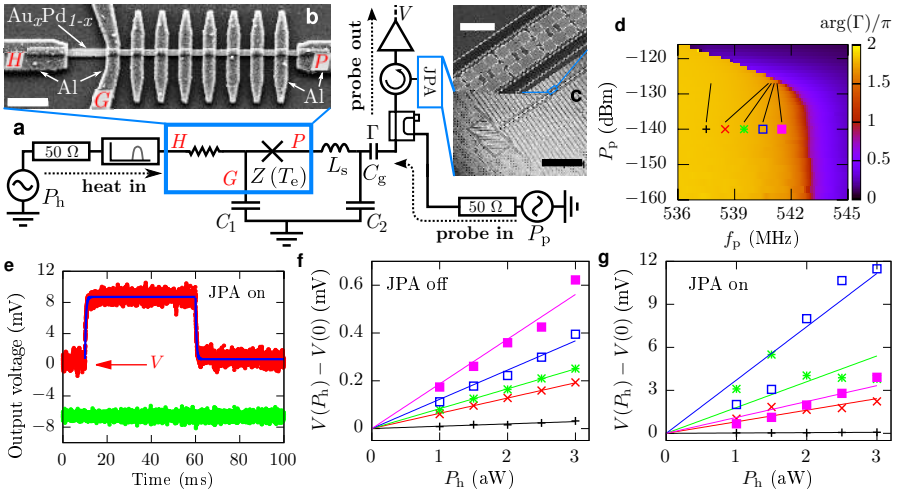

Figure 6.1. Measurement setup and device characterization. **a–c**, Simplified detector measurement setup (**a**) together with micrographs of the superconductor–normal-metal–superconductor (SNS) junctions between leads H, G, and P (**b**) and of a Josephson parametric amplifier (JPA) (**c**). The images are taken from a device similar to the measured. The impedance $Z(T_e)$ of the array of short SNS junctions forms a temperature-sensitive resonant circuit together with a meander inductor $L_s \approx 1.2$ nH and the capacitors $C_1 \approx 87$ pF and $C_2 \approx 33$ pF. The gate capacitance is $C_g \approx 0.87$ pF. There is an 8.4-GHz bandpass filter connected to lead H. The scalebar in panel **b** indicates 1 μm and in panel **c** 15 μm (top) and 400 μm (bottom). **d**, Phase of the reflection coefficient at the gate capacitor arg(Γ) as a function of probe frequency f_p and power P_p, without heating and with the JPA off. **e**, Example of the ensemble-averaged detector output voltage at the digitizer V (top curve) and voltage in the orthogonal quadrature (bottom curve), with the JPA on. The blue curves show exponential fits to the rising and falling edges of the signal. **f, g**, Change in the detector output voltage at the digitizer after the heater is turned on (markers, see panel **e**) as a function of the finite heater power P_h with the JPA off (**f**) and on (**g**). The typical 1σ uncertainty of the voltage measurement is of the order of the symbol size. The (f_p,P_p) operation points are indicated in panel **d**. The JPA shifts the resonance frequency slightly, thus the highest response is found at slightly different operation point. The figure is adapted from Publication IV.

This effectively eliminates $1/f$-type noise from the readout, whereas limiting the readout bandwidth reduces white noise-sources. Typical frequencies employed in other cQED devices are an order of magnitude higher, which further prevents the unwanted back action caused by the probe tone in future applications. The readout frequency is still high enough that commercial off-the-shelf microwave components can be used in the input and output lines. Furthermore, all connections to the nanowire are made through superconductors which suppresses the electronic contribution to the thermal conductance [99].

We detect the change in resonance frequency by measuring the reflection coefficient Γ by reflecting a probe tone off from the gate capacitor C_g at the frequency f_p. The strong temperature dependence is clearly visible in Fig. 6.1d where we show the phase of reflection coefficient Γ as a function of probe power and probe frequency. As the probe power is increased, the probe signal itself begins to heat the nanowire, and the resonance

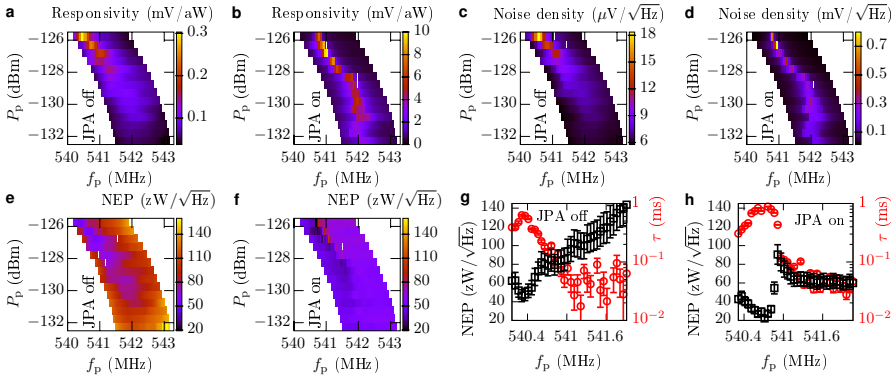

Figure 6.2. Noise equivalent power (NEP) and thermal time constant. **a–d**, Quasistatic responsivity of the probe voltage to the heater power (**a, b**) and probe voltage spectral density (**c, d**) as functions of probe frequency and power with the Josephson parametric amplifier (JPA) off (**a, c**) and on (**b, d**) averaged over noise frequencies between 20 and 100 Hz. **e, f**, Noise equivalent power as a function of the probe frequency and power with the JPA off (**e**) and on (**f**) averaged over noise frequencies between 20 and 100 Hz. **g, h**, NEP (black) and thermal time constant (red) with the JPA off at fixed $P_p = -126$ dBm (**g**) and with the JPA on at $P_p = -126.5$ dBm (**h**). The error bars indicate the standard error of the mean for the time constant and the error arising from the heater power calibration for NEP. The figure is adapted from Publication IV.

frequency shifts to lower frequencies. We also have an option to further amplify the readout signal with a Josephson parametric amplifier [82] shown in Fig. 6.1c.

Figure 6.1e shows an example of the basic measurement used in the characterization of a bolometer. The probe signal is turned on at time $t = 0$. After a delay of 10 ms, the heating pulse lasting for 50 ms is applied through lead H. The recorded output voltage increases exponentially towards the steady-state value as the heater is turned on. Similarly, once the heater is turned off, the output voltage drops exponentially to its initial value. From this data, we extract several key characteristics of the bolometer. The response of the bolometer is defined as the difference in output voltage with the heater on and off. The measured response at a few different operation points is shown in Fig. 6.1f,g. The bolometer quasistatic responsivity is defined as response divided by the heating power. Furthermore, the thermal time constant τ is obtained from the rise time of the output voltage.

The key characteristic performance indicators of the device are shown in Fig. 6.2 with and without the JPA. As the probe power is increased, the resonance becomes sharper which leads to an increase in the responsivity as shown in Fig. 6.2a,b. The peak of the responsivity is found at probe frequencies near the resonance frequency. The depth of the resonance dip decreases at very high probe powers, thus there is an optimal operation point in (f_p, P_p) plane. We also measure the noise spectral density as a function of the probe power and frequency. The results are shown in Fig. 6.2c,d. The background noise far off-resonance, and at low probe

powers, is set by the noise arising from the amplification chain. However, with the JPA on, we consistently observe an increase in the noise density even at very low probe powers indicating that the spectrum near the resonance is dominated by the intrinsic noise of the bolometer.

Figure 6.2e,f shows the NEP as a function of the probe power and frequency. We define the noise equivalent power as output voltage spectral density divided by the quasistatic responsivity and multiplied by the factor $\sqrt{1+(2\pi\tau f_{\mathrm{n}})^2}$, which takes into account the finite rise time of the response. Here, f_{n} is the noise frequency. Note, that the color scale is identical in Figs. 6.2e and 6.2f, which highlights the benefit of low-noise amplification.

The NEP and the corresponding time constant as functions of the probe frequency at the optimal probe power are shown in Fig. 6.2g, h. Note that the frequency for the minimum NEP coincides with that of the maximum thermal time constant. This indicates that the lowest NEP is obtained at a probe frequency slightly below the resonance where the electrothermal feedback is strongly positive. The lowest measured NEP without the JPA is around 50 zW/$\sqrt{\mathrm{Hz}}$ which drops to roughly 20 zW/$\sqrt{\mathrm{Hz}}$ with the JPA turned on. Interestingly, the NEP away from the resonance remains relatively flat at 60 zW/$\sqrt{\mathrm{Hz}}$ with the JPA on indicating that the thermal fluctuations of the bolometer dominate the noise spectrum instead of the amplifier noise. This provides the possibility of using the bolometer over an order of magnitude faster than at the optiman NEP point with relatively low impact on the performance since the thermal time constant drops sharply at frequencies slightly above the its maximum point.

The upper bound for single-photon energy resolution can be calculated from the NEP with equation [100]

$$\epsilon \approx \left(\int_0^\infty \frac{4\mathrm{d}f}{\mathrm{NEP}(f)^2} \right)^{-1/2}.$$

In practice, we restrict the integral to frequencies below the thermal-cutoff frequency $1/(2\pi\tau)$. The finest energy resolution is found with the JPA on at $P_{\mathrm{p}} = -126.5$ dBm and $f_{\mathrm{p}} = 541.9625$ MHz yielding $\epsilon = 0.32$ zJ $= h \times 480$ GHz. If the cutoff frequency is increased to 10 kHz, the estimate for the finest energy resolution becomes $\epsilon = 0.26$ zJ $= h \times 390$ GHz.

6.2 Graphene bolometer

Graphene is a promising candidate for the bolometer absorber and thermometer material thanks to its two-dimensional structure, and hence low heat capacity. Furthermore, the charge carrier density of graphene can be controlled with an electric field which may improve the performance of our bolometer which is sensitive only to the electron temperature.

In Publication V, we study a graphene-based bolometer. The device is

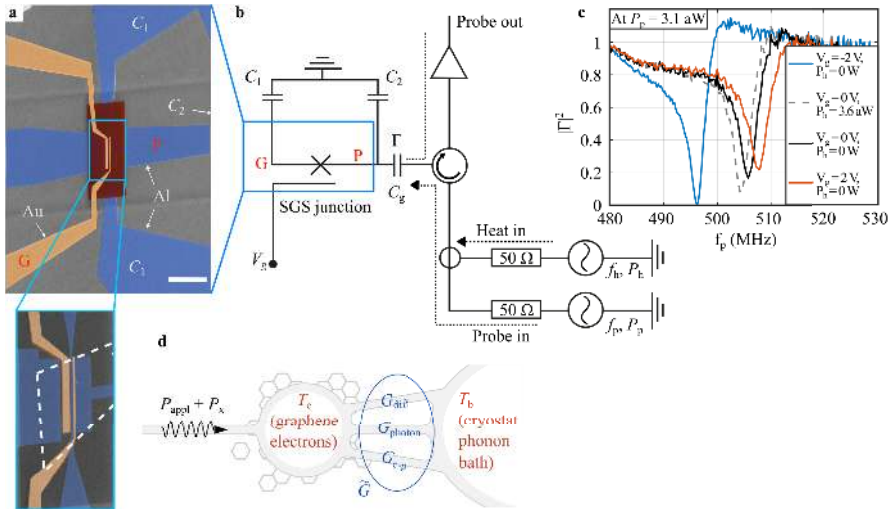

Figure 6.3. Graphene-based bolometer and its operation principle. **a**, False-color scanning-electron-microscope (SEM) image of the graphene bolometer. The scale bar denotes 10 µm. The gate voltage is applied at port G whereas the heater and probe signals couple through port P to the superconductor–graphene–superconductor (SGS) junction formed between the aluminum (blue color) electrodes of port P and of the capacitor C_1. The extent of the graphene flake is indicated by the white dashed line in the inset where we do not show the gate insulator (red color) for clarity. The leftmost aluminum and gold (orange color) electrodes are not used in this work. **b**, Circuit diagram of the detector and a simplified measurement setup. The heater and probe signals, denoted by subscripts h and p, respectively, are combined at room temperature. The microwave reflection coefficient for the probe tone is denoted by Γ. **c**, Reflected fraction of the probe power P_p as a function of the probe frequency f_p for the indicated gate voltages V_g and heater powers P_h at the bath temperature $T_b = 55$ mK. **d**, Considered thermal model. The electrons in the graphene are coupled to the cryostat phonons through an effective thermal conductance $\tilde{G} = G_{e-p} + G_{diff} + G_{photon}$ which is a sum of the phononic (G_{e-p}), electron diffusion (G_{diff}), and photonic (G_{photon}) contributions. Figure adapted from Publication V.

similar to the one studied in Publication IV with three notable exceptions. Firstly, the gold-palladium nanowire is replaced with monolayer graphene. Secondly, we have only a single Josephson junction instead of eight due to the higher inductance of the superconductor–graphene–superconductor (SGS) junction. Finally, we fabricate a gate electrode on top of the junction, with which we can change the charge carrier density. The measurement scheme is otherwise identical to the one in Publication IV with the exception that the heating pulse is applied through the same line as the probe signal. The device is shown in Fig. 6.3a,b together with a simplified measurement scheme.

Figure 6.3c shows a few examples of reflection coefficient Γ measured with different heating powers and gate voltages. We observe that the resonance shifts with the heating signal as expected, and importantly, it can be shifted also with the gate voltage. The total shift of the resonance frequency we measure with gate voltages ±20 V is up to about 80 MHz.

Figure 6.3d shows the considered thermal model. The electrons in the

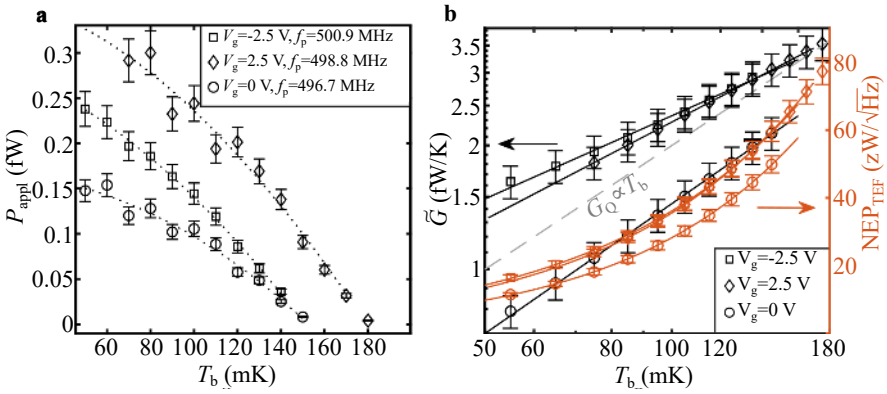

Figure 6.4. Sample thermal conductance characterization data. **a**, Measured points of constant resonance frequency (markers) in the plane of the cryostat phonon temperature, T_b, and the absorbed power in the graphene, P_{appl}, for the indicated gate voltages and probe frequencies. The dotted lines represent polynomial fits to the data. **b**, Differential thermal conductance of the graphene electron system (black markers), $\tilde{G}$, as a function of T_b obtained by differentiating the polynomial fits in **a** with respect to T_b at the temperature points of the measured data. The black solid lines are fits to the markers linear on the logarithmic scale. The grey dashed line shows 2.0% of the quantum of the thermal conductance G_Q. The red markers and lines show the thermal-fluctuation-limited noise equivalent power NEP$_{TEF}$ (right vertical axis) corresponding to the differential thermal conductance shown in black color. The error bars denote 1σ confidence intervals. Figure adapted from Publication V.

graphene thermalize to the phonon bath in this model through three channels: electtron–phonon coupling, electron diffusion, and electron–photon coupling. We measure the differential thermal conductance $\tilde{G}$ by measuring how much heating power P_{appl} we need to apply to the sample in order to keep the resonance frequency constant for a changing bath temperatures T_b as shown in Fig. 6.4a. Differential thermal conductance is obtained from the derivative of the isothermal curve in the (T_b, P_{appl}) plane. The results are shown in Fig. 6.4b.

Although we can only measure the total thermal conductance, we note that it scales roughly linearly with the bath temperature. This indicates that the photonic thermal conductance [101] is dominating, since the phononic contribution scales as the bath temperature to the power ranging from 2 to 4 [102–106]. Electron diffusion also seems unlike due to the utilized superconducting leads that suppress this effect [99].

Let us discuss the performance of the graphene bolometer. The noise equivalent power and the thermal time constant are shown in Fig. 6.5a–c as functions of the probe frequency at a few different gate voltages. The minimum NEP is found at zero gate voltage where it reads 30zW/$\sqrt{\text{Hz}}$, on par with the results of Publication IV. However, the thermal time constant we find is two orders of magnitude shorter. At the most sensitive point, the thermal time constant is 500 ns, and the minimum observed value is around 200 ns. Thus, the integral of Eq. (6.1) can be carried out to much

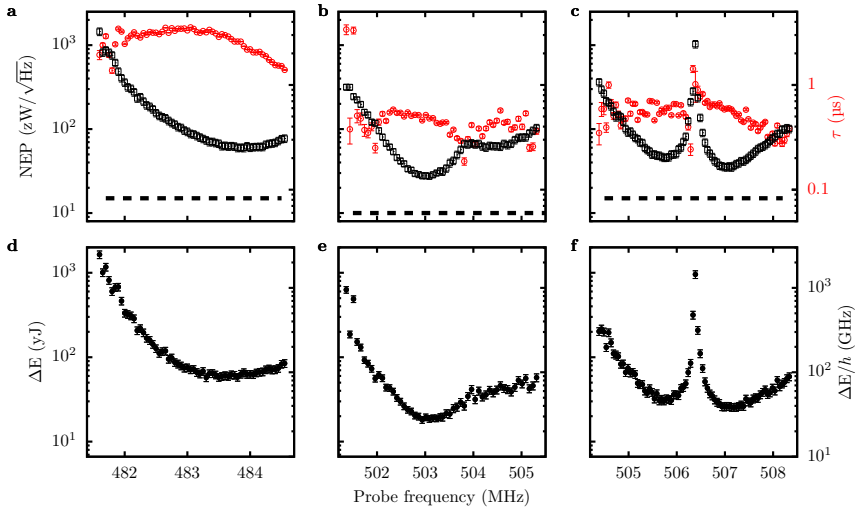

Figure 6.5. Key performance indicators of the graphene bolometer. **a–c**, Measured noise equivalent power (NEP) (black markers, left axis) and thermal relaxation time τ (red markers, right axis) of the detector for gate voltages, $V_g = -2.5\,\mathrm{V}$ (**a**), $V_g = 0\,\mathrm{V}$ (**b**), and $V_g = 2.5\,\mathrm{V}$ (**c**), bath temperature $T_b = 55$ mK, and probe power $P_p = 530$ aW (**a**), $P_p = 140$ aW (**b**), and $P_p = 370$ aW (**c**). The dashed horizontal lines indicate the thermal-fluctuation-limited NEPs obtained from the thermal conductance given by Fig. 6.4b. The error bars denote 1σ confidence intervals. **d–f**, Energy resolution of the bolometer obtained from the NEP and time constant experiments of panels **a–c**, respectively. See text for details. Figure adapted from Publication V.

higher frequencies, which leads to a significantly lower energy resolution. The energy resolution as a function of the probe frequency at different gate voltages is shown in Fig. 6.5d–f. The finest energy resolution of 20 yJ $= h \times 30$ GHz coincides with the minimum of the NEP.

Interestingly, a thermal time constant of around 300 ns together with a 0.8-fW/K thermal conductance implies that the heat capacity of the graphene sheet is 2.5×10^{-22}J/K. Thus, we obtain the standard deviation of energy due to thermal fluctuation $\sqrt{\overline{\delta E^2}} = h \times 4.4$ GHz. Therefore, it seems that we could further improve the results by introducing a JPA to the readout amplification chain. If the JPA would provide similar improvement as with the gold-palladium bolometer, the energy resolution would became $h \times 12$ GHz. Even without near-quantum-limited amplification, our bolometer is fast and sensitive enough to be utilized in cQED.

7. Conclusions and outlook

In this thesis, we investigated possible supporting components for the future large-scale superconducting quantum computer. We explored the properties of SNS junctions, which constitute an elementary building block in many superconducting circuits. Furthermore, we demonstrated that Josephson junctions can be used as a microwave phase shifter, a device that may allow one to realize a single-chip vector signal generator operating at cryogenic temperatures.

The main focus of this dissertation was on bolometry. We characterized an SNS-junction-based bolometer, which we found to surpass the performance of mature thermal detection technologies, such as transition-edge sensors. Integration of a near-quantum-limited amplifier was found to further improve the results by about a factor of three. Far greater improvement was achieved by using graphene as the sensor material for the bolometer. We demonstrated high sensitivity promoting thermal detectors compatible with certain applications in cQED.

The properties of SNS junctions were studied in Publication I. Here, we introduced a technique for measuring the microwave admittance of SNS junctions. It relies on grounding a half-wave resonator through a chain of SNS junctions arranged into SQUID loops. By measuring the resonance frequencies and quality factors of the resonator modes, we were able to determine the admittance of the junctions. We found that our experimental results do not agree with the theoretical predictions of the Usadel equations. We were unable to determine the exact reason for the discrepancy. Thus, in the future, it may be fruitful to study normal metals which are known to behave nearly ideally at dc, such as copper, instead of the gold-palladium alloy used here.

Publication II introduced and demonstrated a flux-tunable phase shifter for microwaves and its operation over wide bandwidth was shown in Publication III. It consists of a transmission line interrupted by three equidistant SQUIDs. We showed that such a system can tune the phase of a signal with vanishing reflections. The operation was experimentally verified at a frequency of 6.3 GHz. Our theoretical considerations suggested a large tun-

ability over a broad frequency range. In the future, the phase shifter may be integrated with a Josephson-junction-based microwave photon source, thus creating an on-chip signal generator. This would allow shift from the use of bulky room temperature instruments into those operating in a cryostat, possibly aiding in scaling up the superconducting quantum computer. However, the phase shifter itself can still be developed further. For example, the tunability range may be increased by adding more SQUIDs to the phase shifter.

The core of this thesis focused on bolometers operating at microwave frequencies. In Publication IV, we characterized an SNS-junction-based bolometer. We connected a capacitor in parallel with a chain of SNS junctions, thus forming an LC oscillator, resonance frequency of which acted as our thermometer. We thermally coupled the junctions to a 36-Ω resistor serving as an absorber of microwave radiation. We found a record-breaking NEP for thermal detectors and by supplementing the measurement circuitry with a near-quantum-limited amplifier, the results were improved by about a factor of three. Further improvement may be achieved by decreasing the size of the absorbing element, or by fabricating it out of metal with lower heat capacity. The predicted energy resolution can be verified by coupling the bolometer to a terahertz antenna, and using a black body as a source of photons, work that we have already begun.

Finally, we introduced a graphene-Josephson-junction-based bolometer in Publication V. As for the SNS bolometer, we connected a capacitor in parallel with the junction and employed the resulting LC resonance as a thermometer. However, the microwave radiation was absorbed directly by the thermometer junction. We found an NEP on par with our SNS-junction-based bolometer. More importantly, the thermal time constant was measured to be two orders of magnitude shorter, which indicates an order of magnitude improvement to the energy resolution bringing it down to $h \times 30$ GHz. Thus, we were able to advance bolometers to the threshold for cQED which lies in the $h \times 10$-GHz 100-ns rage for typical qubit readout schemes. In the future, the implementation of the bolometer may be unified with that in Publication IV in order to allow independent readout and detection absorption lines. The performance could be further improved by introducing a near-quantum-limited amplifier to the readout. Furthermore, fabrication techniques need to be refined for applications beyond this initial proof-of-concept.

References

1. Langley, S. P. *The bolometer and radiant energy.* in *Proceedings of the American Academy of Arts and Sciences* **16** (1880), 342.
2. Onnes, H. K. *Further experiments with liquid helium.* in *Proceedings of the KNAW* **13** (1911), 1910.
3. Josephson, B. D. "Possible new effects in superconductive tunnelling". *Phys. Lett.* **1,** 251 (1962).
4. Clarke, J. & Wilhelm, F. K. "Superconducting quantum bits". *Nature* **453,** 1031 (2008).
5. Martinis, J. M. "Superconducting phase qubits". *Quantum Inf. Process.* **8,** 81 (2009).
6. Fedorov, K. G., Shcherbakova, A. V., Wolf, M. J., Beckmann, D. & Ustinov, A. V. "Fluxon Readout of a Superconducting Qubit". *Phys. Rev. Lett.* **112,** 160502 (2014).
7. Feynman, R. P. "Simulating Physics with Quantum Computers". *Int. J. Theor. Phys.* **21,** 467 (1982).
8. Simon, D. R. "On the power of quantum computation". *SIAM J. Comput.* **26,** 1474 (1997).
9. Childs, A. M. & Van Dam, W. "Quantum algorithms for algebraic problems". *Rev. Mod. Phys.* **82,** 1 (2010).
10. Houck, A. A., Türeci, H. E. & Koch, J. "On-chip quantum simulation with superconducting circuits". *Nat. Phys.* **8,** 292 (2012).
11. Arute, F. *et al.* "Quantum supremacy using a programmable superconducting processor". *Nature* **574,** 505 (2019).
12. Yeh, J.-H., LeFebvre, J., Premaratne, S., Wellstood, F. C. & Palmer, B. S. "Microwave attenuators for use with quantum devices below 100 mK". *J. Appl. Phys.* **121,** 224501 (2017).
13. Naaman, O. *et al.* "Josephson junction microwave modulators for qubit control". *J. Appl. Phys.* **121,** 073904 (2017).

14. Pechal, M. *et al.* “Superconducting Switch for Fast On-Chip Routing of Quantum Microwave Fields”. *Phys. Rev. Appl.* **6,** 024009 (2016).

15. Abdo, B., Brink, M. & Chow, J. M. “Gyrator Operation Using Josephson Mixers”. *Phys. Rev. Appl.* **8,** 034009 (2017).

16. Sliwa, K. M. *et al.* “Reconfigurable Josephson Circulator/Directional Amplifier”. *Phys. Rev. X* **5,** 041020 (2015).

17. Cassidy, M. *et al.* “Demonstration of an ac Josephson junction laser”. *Science* **355,** 939 (2017).

18. Houck, A. A. *et al.* “Generating single microwave photons in a circuit”. *Nature* **449,** 328 (2007).

19. Peng, Z., De Graaf, S., Tsai, J. & Astafiev, O. “Tuneable on-demand single-photon source in the microwave range”. *Nat. Commun.* **7,** 12588 (2016).

20. George, R. *et al.* “Multiplexing Superconducting Qubit Circuit for Single Microwave Photon Generation”. *J. Low Temp. Phys.* **189,** 60 (2017).

21. Romero, G., García-Ripoll, J. J. & Solano, E. “Photodetection of propagating quantum microwaves in circuit QED”. *Phys. Scr.* **2009,** 014004 (2009).

22. Romero, G., García-Ripoll, J. J. & Solano, E. “Microwave Photon Detector in Circuit QED”. *Phys. Rev. Lett.* **102,** 173602 (2009).

23. Chen, Y.-F. *et al.* “Microwave Photon Counter Based on Josephson Junctions”. *Phys. Rev. Lett.* **107,** 217401 (2011).

24. Peropadre, B. *et al.* “Approaching perfect microwave photodetection in circuit QED”. *Phys. Rev. A* **84,** 063834 (2011).

25. Fan, B. *et al.* “Breakdown of the cross-Kerr scheme for photon counting”. *Phys. Rev. Lett.* **110,** 053601 (2013).

26. Hoi, I.-C. *et al.* “Giant cross-Kerr effect for propagating microwaves induced by an artificial atom”. *Phys. Rev. Lett.* **111,** 053601 (2013).

27. Sathyamoorthy, S. R. *et al.* “Quantum Nondemolition Detection of a Propagating Microwave Photon”. *Phys. Rev. Lett.* **112,** 093601 (2014).

28. Fan, B., Johansson, G., Combes, J., Milburn, G. J. & Stace, T. M. “Nonabsorbing high-efficiency counter for itinerant microwave photons”. *Phys. Rev. B* **90,** 035132 (2014).

29. Koshino, K., Inomata, K., Lin, Z., Nakamura, Y. & Yamamoto, T. “Theory of microwave single-photon detection using an impedance-matched Λ system”. *Phys. Rev. A* **91,** 043805 (2015).

30. Narla, A. *et al.* “Robust concurrent remote entanglement between two superconducting qubits”. *Phys. Rev. X* **6,** 031036 (2016).

31. Inomata, K. *et al.* “Single microwave-photon detector using an artificial Λ-type three-level system”. *Nat. Commun.* **7,** 12303 (2016).
32. Harmon, S. A. & Cheville, R. A. “Part-per-million gas detection from long-baseline THz spectroscopy”. *Appl. Phys. Lett.* **85,** 2128 (2004).
33. Woodward, R. M. “Terahertz technology in global homeland security”. *Proc. SPIE* **5781,** 22 (2005).
34. Woolard, D. L., Brown, E. R., Pepper, M. & Kemp, M. “Terahertz frequency sensing and imaging: A time of reckoning future applications?” *Proc. IEEE* **93,** 1722 (2005).
35. Stevens, J. R. *et al.* “Characterization of Transition Edge Sensors for the Simons Observatory.” *J. Low Temp. Phys.* **199,** 672 (2020).
36. Pickwell, E. & Wallace, V. P. “Biomedical applications of terahertz technology”. *J. Phys. D* **39,** R301 (2006).
37. Irwin, K. D. “An application of electrothermal feedback for high resolution cryogenic particle detection”. *Appl. Phys. Lett.* **66,** 1998 (1995).
38. Ullom, J. N. & Bennett, D. A. “Review of superconducting transition-edge sensors for x-ray and gamma-ray spectroscopy”. *Supercond. Sci. Technol.* **28,** 084003 (2015).
39. Revéret, V. *et al.* “HERSCHEL—PACS Bolometer Arrays for Submillimeter Ground-Based Telescopes”. *J. Low Temp. Phys.* **151,** 32 (2008).
40. Jackson, B. D. *et al.* “The SPICA-SAFARI Detector System: TES Detector Arrays With Frequency-Division Multiplexed SQUID Readout”. *IEEE Trans. Terahertz Sci.* **2,** 12 (2011).
41. Karasik, B. S., Sergeev, A. V. & Prober, D. E. “Nanobolometers for THz Photon Detection”. *IEEE Trans. Terahertz Sci.* **1,** 97 (2011).
42. Hochberg, Y., Lin, T. & Zurek, K. M. “Detecting ultralight bosonic dark matter via absorption in superconductors”. *Phys. Rev. D* **94,** 015019 (2016).
43. Krauss, L., Moody, J., Wilczek, F. & Morris, D. E. “Calculations for cosmic axion detection”. *Phys. Rev. Lett.* **55,** 1797 (1985).
44. Anastassopoulos, V. *et al.* “New CAST limit on the axion–photon interaction”. en. *Nat. Phys.* **13,** 584 (2017).
45. McAllister, B. T. *et al.* “The ORGAN experiment: An axion haloscope above 15 GHz”. *Phys. Dark Universe* **18,** 67 (2017).
46. Tan, S.-H. *et al.* “Quantum Illumination with Gaussian States”. *Phys. Rev. Lett.* **101,** 253601 (2008).
47. Las Heras, U. *et al.* “Quantum illumination reveals phase-shift inducing cloaking”. *Sci. Rep.* **7,** 9333 (2017).

48. Takahashi, H. *et al.* “Entanglement distillation from Gaussian input states”. *Nat. Photon.* **4,** 178 (2010).

49. Govenius, J., Matsuzaki, Y., Savenko, I. G. & Möttönen, M. “Parity measurement of remote qubits using dispersive coupling and photodetection”. *Phys. Rev. A* **92,** 042305 (2015).

50. Govia, L. C. G. *et al.* “High-fidelity qubit measurement with a microwave-photon counter”. *Phys. Rev. A* **90,** 062307 (2014).

51. Opremcak, A. *et al.* “Measurement of a superconducting qubit with a microwave photon counter”. *Science* **361,** 1239 (2018).

52. Karasik, B. S. & Cantor, R. “Demonstration of high optical sensitivity in far-infrared hot-electron bolometer”. *Appl. Phys. Lett.* **98,** 193503 (2011).

53. De Visser, P. J., Baselmans, J. J. A., Bueno, J., Llombart, N. & Klapwijk, T. M. “Fluctuations in the electron system of a superconductor exposed to a photon flux”. *Nat. Commun.* **5,** 3130 (2014).

54. Echternach, P. M., Pepper, B. J., Reck, T. & Bradford, C. M. “Single photon detection of 1.5 THz radiation with the quantum capacitance detector”. *Nat. Astron.* **2,** 90 (2018).

55. Komiyama, S., Astafiev, O., Antonov, V., Kutsuwa, T. & Hirai, H. “A single-photon detector in the far-infrared range”. *Nature* **403,** 405 (2000).

56. Govenius, J. *et al.* “Microwave nanobolometer based on proximity Josephson junctions”. *Phys. Rev. B* **90,** 064505 (2014).

57. Govenius, J., Lake, R. E., Tan, K. Y. & Möttönen, M. “Detection of Zeptojoule Microwave Pulses Using Electrothermal Feedback in Proximity-Induced Josephson Junctions”. *Phys. Rev. Lett.* **117,** 030802 (2016).

58. Karimi, B., Brange, F., Samuelsson, P. & Pekola, J. P. “Reaching the ultimate energy resolution of a quantum detector”. *Nat. Commun.* **11,** 1 (2020).

59. Kono, S., Koshino, K., Tabuchi, Y., Noguchi, A. & Nakamura, Y. “Quantum non-demolition detection of an itinerant microwave photon”. *Nat. Phys.* **14,** 546 (2018).

60. Besse, J.-C. *et al.* “Single-Shot Quantum Nondemolition Detection of Individual Itinerant Microwave Photons”. *Phys. Rev. X* **8,** 021003 (2018).

61. Dassonneville, R., Assouly, R., Peronnin, T., Rouchon, P. & Huard, B. “Number-resolved photocounter for propagating microwave mode”. *Preprint, arXiv:2004.05114* (2020).

62. Suzuki, T. *et al.* “Performance of SAFARI Short-Wavelength-Band Transition Edge Sensors (TES) Fabricated by Deep Reactive Ion Etching”. *IEEE Trans. Terahertz Sci.* **4,** 171 (2014).

63. Efetov, D. K. *et al.* “Fast thermal relaxation in cavity-coupled graphene bolometers with a Johnson noise read-out”. *Nat. Nanotechnol.* **13,** 797 (2018).

64. Blais, A., Grimsmo, A. L., Girvin, S. M. & Wallraff, A. “Circuit Quantum Electrodynamics”. *Preprint, arXiv:2005.12667* (2020).

65. Ambegaokar, V. & Baratoff, A. “Tunneling between superconductors”. *Phys. Rev. Lett.* **10,** 486 (1963).

66. Faivre, T., Golubev, D. & Pekola, J. P. “Josephson junction based thermometer and its application in bolometry”. *J. Appl. Phys.* **116,** 094302 (2014).

67. Dubos, P. *et al.* “Josephson critical current in a long mesoscopic S-N-S junction”. *Phys. Rev. B* **63,** 064502 (2001).

68. Giazotto, F. *et al.* “Ultrasensitive proximity Josephson sensor with kinetic inductance readout”. *Appl. Phys. Lett.* **92,** 162507 (2008).

69. Usadel, K. D. “Generalized Diffusion Equation for Superconducting Alloys”. *Phys. Rev. Lett.* **25,** 507 (1970).

70. Virtanen, P., Bergeret, F. S., Cuevas, J. C. & Heikkilä, T. T. “Linear ac response of diffusive SNS junctions”. *Phys. Rev. B* **83,** 144514 (2011).

71. Virtanen, P. *Nonequilibrium and transport in proximity of superconductors.* PhD thesis, Helsinki University of Technology, Espoo (2009).

72. Meissner, H. “Superconductivity of Contacts with Interposed Barriers”. *Phys. Rev.* **117,** 672 (1960).

73. Andreev, A. F. “Electron spectrum of the intermediate state of superconductors”. *Sov. J. Exp. Theor. Phys.* **22,** 455 (1965).

74. Dubos, P., Courtois, H., Buisson, O. & Pannetier, B. “Coherent low-energy charge transport in a diffusive S-N-S junction”. *Phys. Rev. Lett.* **87,** 206801 (2001).

75. Fagaly, R. L. “Superconducting quantum interference device instruments and applications”. *Rev. Sci. Instrum.* **77,** 101101 (2006).

76. Geng, Z., Helenius, A. P., Heikkilä, T. T. & Maasilta, I. J. “Superconductor-ferromagnet tunnel junction thermoelectric bolometer and calorimeter with a SQUID readout”. *J. Low Temp. Phys.* **199,** 1 (2020).

77. Enss, C. *Cryogenic Particle Detection* (Springer-Verlag Berlin, Heidelberg, 2005).

78. Metzger, G. & Vabre, J. P. *Transmission lines with pulse excitation* (Academic Press, Waltham, MA, 1969).

79. Pozar, D. M. *Microwave engineering* 4th ed. (John wiley & sons, Hoboken, 2011).

80. Richards, P. L. "Bolometers for infrared and millimeter waves". *J. Appl. Phys.* **76,** 1 (1994).

81. Zorin, A. B. "The thermocoax cable as the microwave frequency filter for single electron circuits". *Rev. Sci. Instrum.* **66,** 4296 (1995).

82. Simbierowicz, S. *et al.* "A flux-driven Josephson parametric amplifier for sub-GHz frequencies fabricated with side-wall passivated spacer junction technology". *Supercond. Sci. Technol.* **31,** 105001 (2018).

83. Clarke, J. "Experimental comparison of the Josephson voltage-frequency relation in different superconductors". *Phys. Rev. Lett.* **21,** 1566 (1968).

84. Likharev, K. K. "Superconducting weak links". *Rev. Mod. Phys.* **51,** 101 (1979).

85. Heikkilä, T. T., Särkkä, J. & Wilhelm, F. K. "Supercurrent-carrying density of states in diffusive mesoscopic Josephson weak links". *Phys. Rev. B* **66,** 184513 (2002).

86. Courtois, H., Meschke, M., Peltonen, J. T. & Pekola, J. P. "Origin of Hysteresis in a Proximity Josephson Junction". *Phys. Rev. Lett.* **101,** 067002 (2008).

87. Galaktionov, A. V. & Zaikin, A. D. "Fluctuations of the Josephson current and electron-electron interactions in superconducting weak links". *Phys. Rev. B* **82,** 184520 (2010).

88. Kos, F., Nigg, S. E. & Glazman, L. I. "Frequency-dependent admittance of a short superconducting weak link". *Phys. Rev. B* **87,** 174521 (2013).

89. Ferrier, M., Dassonneville, B., Guéron, S. & Bouchiat, H. "Phase-dependent Andreev spectrum in a diffusive SNS junction: Static and dynamic current response". *Phys. Rev. B* **88,** 174505 (2013).

90. Tikhonov, K. S. & Feigel'man, M. V. "Admittance of a long diffusive SNS junction". *Phys. Rev. B* **91,** 054519 (2015).

91. Chiodi, F. *et al.* "Probing the dynamics of Andreev states in a coherent Normal/Superconducting ring". *Sci. Rep.* **1,** 3 (2011).

92. Dassonneville, B., Ferrier, M., Guéron, S. & Bouchiat, H. "Dissipation and Supercurrent Fluctuations in a Diffusive Normal-Metal–Superconductor Ring". *Phys. Rev. Lett.* **110,** 217001 (2013).

93. Geerlings, K. *et al.* “Improving the quality factor of microwave compact resonators by optimizing their geometrical parameters”. *Appl. Phys. Lett.* **100,** 192601 (2012).

94. Khalil, M. S., Stoutimore, M. J. A., Wellstood, F. C. & Osborn, K. D. “An analysis method for asymmetric resonator transmission applied to superconducting devices”. *J. Appl. Phys.* **111,** 054510 (2012).

95. Shinohara, T., Sato, T. & Taniyama, T. “Surface Ferromagnetism of Pd Fine Particles”. *Phys. Rev. Lett.* **91,** 197201 (2003).

96. Sampedro, B. *et al.* “Ferromagnetism in fcc Twinned 2.4 nm Size Pd Nanoparticles”. *Phys. Rev. Lett.* **91,** 237203 (2003).

97. Jabdaraghi, R. N., Peltonen, J. T., Saira, O.-P. & Pekola, J. P. “Low-temperature characterization of Nb-Cu-Nb weak links with Ar ion-cleaned interfaces”. *Appl. Phys. Lett.* **108,** 042604 (2016).

98. Corruccini, R. J. & Gniewek, J. J. *Specific Heats and Enthalpies of Technical Solids at Low Temperatures: A Compilation from the Literature* (United States Department of Commerce, National Bureau of Standards, Boulder, CO, 1960).

99. Peltonen, J. T. *et al.* “Thermal Conductance by the Inverse Proximity Effect in a Superconductor”. *Phys. Rev. Lett.* **105,** 097004 (2010).

100. Moseley, S. H., Mather, J. C. & McCammon, D. “Thermal detectors as x-ray spectrometers”. *J. Appl. Phys.* **56,** 1257 (1984).

101. Schmidt, D. R., Schoelkopf, R. J. & Cleland, A. N. “Photon-Mediated Thermal Relaxation of Electrons in Nanostructures”. *Phys. Rev. Lett.* **93,** 045901 (2004).

102. Chen, W. & Clerk, A. A. “Electron-phonon mediated heat flow in disordered graphene”. *Phys. Rev. B* **86,** 125443 (2012).

103. El Fatimy, A. *et al.* “Effect of defect-induced cooling on graphene hot-electron bolometers”. *Carbon* **154,** 497–502 (2019).

104. Laitinen, A. *et al.* “Electron–Phonon Coupling in Suspended Graphene: Supercollisions by Ripples”. *Nano Lett.* **14,** 3009 (2014).

105. Song, J. C. W., Reizer, M. Y. & Levitov, L. S. “Disorder-Assisted Electron-Phonon Scattering and Cooling Pathways in Graphene”. *Phys. Rev. Lett.* **109,** 106602 (2012).

106. Betz, A. C. *et al.* “Supercollision cooling in undoped graphene”. *Nat. Phys.* **9,** 109 (2013).

Errata

Publication II

In Equation (4), ϕ should read φ.

Aalto-DD 203/2020

ISBN 978-952-64-0170-6 (printed)
ISBN 978-952-64-0171-3 (pdf)
ISSN 1799-4934 (printed)
ISSN 1799-4942 (pdf)

Aalto University
School of Science
Department of applied physics
www.aalto.fi

BUSINESS +
ECONOMY

ART +
DESIGN +
ARCHITECTURE

SCIENCE +
TECHNOLOGY

CROSSOVER

**DOCTORAL
DISSERTATIONS**